Ab-initio simulation of spin-vibronic spectra of methoxy radical

Ketan Sharma*[1], Oleg A. Vasilyev†[2], John F. Stanton‡[1], and Terry A. Miller§[2]

[1]Department of Chemistry, University of Florida, Gainesville, FL 32611, U.S.A.

[2]Department of Chemistry and Biochemistry, The Ohio State University, Columbus, OH 43210, U.S.A.

April 22, 2025

*email: ketan.sharma@ufl.edu

†email: vasilyev.4@osu.edu

‡Deceased - March 21, 2025

§Corresponding author; email: tamiller@chemistry.ohio-state.edu

Abstract

Despite the fact that experimental and theoretical work on the spectrum of methoxy has stretched from the microwave to the ultraviolet and proceeded for nearly 50 years, parts of the spectrum have remained a challenge to simulate theoretically and make reliable line-by-line assignments. The spectral complexity arises because the radical has a non-zero electron spin and significant vibronic coupling between the two electronic components of the ground state due to the presence of a conical intersection. This work describes a completely *ab initio* effort to understand and assign the spin-vibronic levels of the $\tilde{X}\,^2E$ state from 0 to above 3000 cm^{-1}, a region that includes the fundamental transitions of the C-H symmetric and asymmetric stretches that have not previously been identified uniquely. A potential energy surface for methoxy was calculated at the EOM-CCSDT/ANO1 level of theory. Subsequently this potential energy surface was fit to a quartic power series expansion of all nine vibrational normal coordinates (as determined at the minimum of the conical intersection) by the use of a machine-learning-based algorithm. After the addition of spin-orbit coupling, the spin-vibronic problem was solved using both the Krylov-Schur and Lanczos algorithms with the SOCJT3 software to converge eigenvalues up to 3500 cm^{-1} and their eigenvectors. The latter were used, in conjunction with the calculated dipole moment and its derivatives (calculated using finite differences at EOM-CCSDT/ANO1 level), to determine spectral intensities for the spin-vibronic spectra. The calculated transition frequencies and intensities were used to simulate and assign the observed transitions of the spin-vibronic spectra of the radical. The credibility of the assignments and their significance is discussed in detail.

1 Introduction

The methoxy radical (CH_3O) is an important intermediate in combustion[1] and atmospheric chemistry[2], particularly in the oxidation of methane and other hydrocarbons. The spectroscopy of methoxy have an extensive history as shown by both theoretical and experimental studies. Nonetheless, understanding its spin-vibronic structure is challenging due to the complexities introduced by vibronic coupling in the vicinity of the conical intersection. Works, such as the studies by Endo et al. using microwave spectroscopy [3], provided detailed data on the rotational structure of methoxy but focused mainly on the vibrationless level of the ground $\tilde{X}\,^2E$ electronic state.

The methoxy radical has been subject to numerous other experimental studies [4, 5, 6, 7, 8, 9, 10, 11, 12, 13, 14, 15, 16, 17, 18, 19, 20] in the past. Laser-excited, dispersed fluorescence experiments [5, 21, 7, 15, 16] have observed levels with spin-vibronic energies up to 3000 cm^{-1} above the vibrationless $\tilde{X}\,^2E$ level, but with relatively low resolution. Stimulated emission pumping (SEP) spectroscopy [22, 23, 24, 25, 26, 27, 28] improved the resolution.

Photo-electron spectra using the slow-electron velocity-map imaging (SEVI) technique [29], which observed transitions up to 2500 cm^{-1}, has also provided valuable experimental insights. However, for our present purposes the infrared absorption of methoxy in a hydrogen matrix [30] is the single most important experimental benchmark, because of its breadth and continuous coverage.

Correspondingly, numerous theoretical studies [31, 32, 33, 34, 35, 36, 37, 30] have focused on the vibrational dynamics and spectroscopic features of methoxy (CH_3O) and its deuterated counterpart CD_3O, particularly with regards to Jahn-Teller and spin-orbit coupling effects. In 2010, Nagesh et al. analyzed the large-amplitude vibrational dynamics of methoxy on the $\tilde{X}\,^2E$ ground state using a model Hamiltonian, highlighting the influence of conical intersections and surface crossings on vibrational modes [36]. In 2012, further analysis of the infrared spectra of methoxy in the CH stretch region was conducted, showing

that Jahn-Teller coupling and Fermi resonances played key roles [37]. Further, in 2014, researchers simulated the laser-induced fluorescence (LIF) excitation spectrum of CH_3O and CD_3O using vibronic Hamiltonians and Van Vleck perturbation theory, aligning theoretical predictions with experimental results and emphasizing the importance of the interactions between electronic and vibrational states [38].

Later, Weichman et al. [29] used *ab initio* methods to map the low-lying vibronic levels of methoxy. Their study showed that a quadratic expansion of the potential energy surface (PES) was not adequate for describing the structure of methoxy at higher vibrational energies. They applied equation-of-motion coupled-cluster (EOM-CC) methods with a quartic anharmonic potential and a quadratic Jahn-Teller potential to provide more accurate predictions of the photo-electron spectra of methoxy. This work underscored the necessity for higher-order expansions of the PES and more detailed treatments of the Jahn-Teller effect, especially in the CH-stretch region.

Recent advancements [39, 40, 41] in fundamental theory, the effectiveness of algorithms, as well as the size of spin-vibronic problems that can be dealt with [42] have enabled us to do a complete ab-initio simulation of the spin-vibronic structure of the methoxy radical in its ground electronic state. This, in addition to our new machine-learning based method to generate a higher order ab-initio potential, allow for the inclusion of full-quartic vibronic coupling which, along with the incorporation of spin-orbit coupling, thereby makes it possible to simulate and assign spectral transitions beyond 2000 cm^{-1} with greater accuracy than previously. In this work, we aim to utilize these cutting-edge computational techniques to simulate the spin-vibronic spectrum of methoxy up to beyond 3000 cm^{-1}. The quartic expansion of the vibronic Hamiltonian is employed, and combined with the symmetry properties of the C_{3v} point group to reduce the number of independent parameters in the analytical expansion of the electronic potential. Spin-orbit coupling is also incorporated to further enhance the accuracy of spectral assignments. By comparing these theoretical results with experimental data, including spin-orbit splittings and A_1-A_2 separations, this work seeks to provide a comprehensive understanding of the spin-vibronic structure of methoxy.

2 Theory

In this section, we outline the theoretical and computational methods used to simulate and analyze the observed spectra. The calculations are divided into three main components: i) computation and fitting of the potential energy surface (PES) for the methoxy radical, ii) solving the vibronic and spin-vibronic coupling problem, and iii) calculating the transition dipole moments for the spectral analysis.

The two-state Hamiltonian for the methoxy radical in the quasidiabatic basis is expressed as

$$\hat{H} = \begin{bmatrix} T_{11} & 0 \\ 0 & T_{22} \end{bmatrix} + \begin{bmatrix} V_{11} & V_{12} \\ V_{12} & V_{22} \end{bmatrix} \tag{1}$$

where $T_{i,j}$ denotes matrix elements of the nuclear, kinetic energy (presently only vibrational contributions). The potential energy terms, $V_{i,j}$, in this Hamiltonian can be expanded as a Taylor series in terms of normal coordinates (q_i) defined at the conical intersection (CI) at R_0:

$$V_{ij} = \sum_{\alpha \geq 0} \frac{1}{\alpha!} f_{ij}^{\alpha_1 \alpha_2 \ldots \alpha_n} \, q_1^{\alpha_1} q_2^{\alpha_2} \ldots q_n^{\alpha_n} \tag{2}$$

where i and j subscripts enumerate electronic basis state functions.

In our earlier work [43] on the methoxy radical, we used a quadratic potential expansion with the coefficients $f_{ij}^{\alpha_1 \alpha_2 \ldots \alpha_n}$ determined by the derivatives of the electronic Hamiltonian, $\hat{H}_e$, with respect to the normal coordinates q_i, defined for the average of the two degenerate electronic states at the CI. This approach proved insufficient for analyzing spectra, particularly in the 2000-3000 cm^{-1} range [29]. To improve the vibronic Hamiltonian beyond the quadratic approximation, we employed a machine-learning-based approach to fit the adiabatic PES to the form described in Eqs. (1 and 2). In this study, we include all normal modes and truncate the Taylor expansion of the potential energy terms at the quartic order. By utilizing the symmetry properties of the C_{3v} point group, the number of parameters for a complete quartic Hamiltonian fit is reduced to 392 independent parameters.

We generated 5000 random points within the $\leq$ 10000 cm^{-1} region around the CI,

and computed adiabatic energies for the two components of the ground electronic state using the frozen core equation-of-motion ionization potential coupled cluster singles doubles and triples (FC-EOMIP-CCSDT) method with a triple-zeta atomic natural orbital (ANO1) basis. Due to the high dimensionality of the problem at hand i.e. 9 vibrational modes for methoxy, it was impractical to do a systematic scan of the PES. As an example, if one opted to calculate a grid with 4 perturbations along each vibrational mode, the number of single point electronic structure calculations one would need to run would be greater than 200000. With random scans of PESs, we were able to fit the same potential with much lesser number of points. The coefficients in the potential part of $\hat{H}$ were then fitted to these adiabatic energies using a combination of low-memory Broyden–Fletcher–Goldfarb–Shanno (l-BFGS) and adaptive moment (ADAM) optimization algorithms. This fitting resulted in a root mean square error of 1.73 cm^{-1} between the calculated adiabatic energies and the eigenvalues of the potential part of $\hat{H}$. The supplementary material includes a table listing the values of all fitted parameters $f_{ij}^{\alpha_1\alpha_2\cdots\alpha_n}$. Full details of the fitting procedure will be provided in a forthcoming publication.

In addition to vibronic couplings, spin-orbit coupling is also incorporated into the calculations. The spin-orbit operator is of the form:

$$\hat{H}_{SO} = a_{\parallel}\hat{L}_z\hat{S}_z \tag{3}$$

Of course a general spin-orbit operator would also have components perpendicular to z. However, Watson[44] and others[45, 46] have shown these to vanish within a degenerate electronic state due to the requirements of Hermitian conjugation and time-reversal symmetry.

In the cylindrical representation, we can split the potential part of Eq. (1) into two parts

and combine it with Eq. (3) to form a spin-vibronic Hamiltonian,

$$\hat{H} = \begin{bmatrix} T_{11} & 0 \\ 0 & T_{22} \end{bmatrix} + \begin{bmatrix} V_{11} & 0 \\ 0 & V_{22} \end{bmatrix} + \lambda \begin{bmatrix} 0 & V_{12} \\ V_{12} & 0 \end{bmatrix} + \begin{bmatrix} A_z & 0 \\ 0 & -A_z \end{bmatrix} \tag{4}$$

where $\hat{H}$ is expressed in a product basis set consisting of electronic orbital and spin kets, $|\Lambda_i\rangle$, $|\Sigma_s\rangle$, and a vibrational factor of the form, $\prod_j |v_j^i\rangle ... \prod_k |v_k^i, l_k^i\rangle$, with $|v_j^i\rangle$ and $|v_k^i, l_k^i\rangle$ representing simple harmonic basis functions, respectively, for non-degenerate and doubly degenerate vibration modes. As discussed in Section 4, we have added the coefficient, λ, to Eq. (4) in order to be able to study the effect of the varying the magnitude of the JT-couplings in the system. For the complete vibronic/spin-vibronic calculations discussed in this Section, λ is always set to 1.

To obtain the form of the last matrix in Eq. (4) from $\hat{H}_{SO}$, one notes that in the chosen representation

$$\langle\Sigma_s| \langle\Lambda_i| \hat{H}_{SO} |\Lambda_i\rangle |\Sigma_s\rangle = \Lambda_i \zeta_e \Sigma_s = \pm(1/2) a_{\parallel} \zeta_e \tag{5}$$

with ζ_e being the value of the orbital angular momentum for either component of the degenerate electronic state. Since the eigenvalues of $\Lambda_i = \pm 1$ and $\Sigma_s = \pm(1/2)$, one obtains the + sign in Eq. (5) if the eigenvalues are of the same sign or - if not. Therefore by defining $A_z = (1/2) a_{\parallel} \zeta_e$, one obtains the ultimate matrix in Eq. (4) for $\Sigma_s = +(1/2)$. The value of A_z at R_0 was calculated to be -66.5 cm^{-1} at EOMIP-CCSD/ANO1 level of theory using degenerate perturbation theory with the EOMIP-CCSD wavefunctions and ANO1 basis. This value is the same as previously reported by Weichman, *et. al.* [29] using the same method of calculation. While other works on methoxy have considered spin-orbit coupling they have typically determined the electronic coupling constant by varying its value to match the experimental splitting of the zero-point level.

Of course one could also chose $\Sigma_s = -(1/2)$, but this produces an equivalent matrix that should be added to the one discussed above with $\Sigma_s = +(1/2)$. However, all matrix

elements between these two blocks vanish because there are no operators in the Hamiltonian that connect the states with $\Sigma_s = +(1/2)$ to -(1/2). The eigenvalues of the two matrices are the same as are the eigenvectors except that the latter differ by containing basis functions with $\Sigma_s = -(1/2)$ rather than $+(1/2)$. Therefore, the blocks can be treated independently and $|\Sigma_s\rangle$ can effectively be treated as an input parameter to the Hamiltonian rather than a quantum state in the basis set.

The spin-vibronic Hamiltonian was built with a basis set formed by including harmonic basis functions for all vibrational modes, ν_i, centered at R_0 (see Table S.1 in the SI) up to

$$|v_1^{max}, v_2^{max}, v_3^{max}, v_4^{max}, v_5^{max}, v_6^{max}\rangle = \{4, 5, 5, 4, 5, 8\} \tag{6}$$

This resulted in a spin-vibronic Hamiltonian of $\approx$ 5.1 million basis functions, which was diagonalised using the lanczos algorithm. The diagonalisation required 2000 lanczos iterations and all energies up to $\approx$ 3100 cm^{-1} were converged to an average of $\approx$ 0.57 cm^{-1} (when compared to a calculation with $\approx$ 41.9 million basis functions). Further computational convergence with respect to number of lanczos iterations was tested, by increasing the number of iterations to 3000 led to less than 0.02 cm^{-1} variation in eigenvalues. It should be noted here that even though a calculation with 41.9 million was done to check the convergence of eigenvalues, it is not possible, at this time, to compute all the eigenvectors with such large basis set due to the high memory requirements ($\approx$ 20TB for RAM) for such a calculation.

The computed spin vibronic eigenvectors (numbered n in increasing order of energy) are a linear combination of the basis functions,

$$|n, \Gamma\rangle = \sum_i |\Sigma = 1/2\rangle\, |\Lambda_i\rangle\, |\tilde{\eta}^i_{n,\Gamma}\rangle \tag{7}$$

where the sum i is over all the electronic basis functions included in the basis set and as we discussed above only the $|\Sigma = +(1/2)\rangle$ functions are included, $|\tilde{\eta}^i_{n,\Gamma}\rangle$ is the vibrational

cofactor defined as

$$|\tilde{\eta}^i_{n,\Gamma}\rangle = \sum_h C^i_h \prod_{k=1}^{3} |v^h_k\rangle \prod_{k=4}^{6} |v^h_k, l^h_k\rangle \tag{8}$$

where C^i_h is an eigenvector expansion coefficient associated with the Λ_i electronic basis component in the $|n, \Gamma\rangle$ spin-vibronic eigenstate, h is an index enumerating all possible combinations of harmonic oscillator eigenfunctions for six modes. Each eigenfunction is labeled by its irreducible representation in the C^2_{3v} double group, Γ, and a number n enumerating the eigenfunctions in the order of increasing eigenvalues, such that $|n, e_{3/2}\rangle$ eigenstates start from $n = 0$ ($|0, e_{3/2}\rangle$ is the ground spin-vibronic state) and $|n, e_{1/2}\rangle$ eigenstates start from $n = 1$. The eigenvalues are listed in Table 3 and the approximate eigenvectors given in Table S.2.

The transition probabilities for IR absorption spectrum intensities are calculated using the eigenvectors Eq. (7) and the parameterized dipole moment operator

$$S_{f\leftarrow 0} = \sum_\alpha |\langle n', \Gamma'| \mu_\alpha |n'', \Gamma''\rangle|^2 \tag{9}$$

where the α subscript denotes z, $+$, and $-$ components of the dipole moment operator in the molecular-fixed coordinate system. The perpendicular cylindrical components can be related to Cartesian ones by

$$\mu_\pm = \frac{1}{\sqrt{2}} (\mu_x \pm \mathrm{i}\mu_y) \tag{10}$$

and μ_z is the same in both systems. Substituting wavefunctions from Eq. (7) and integrating out the spin part, the spin-vibronic transition dipole moment values $\langle n', \Gamma'| \mu_\alpha |n'', \Gamma''\rangle$ between the ground state $|n'', \Gamma''\rangle$ and the final state $|n', \Gamma'\rangle$ can be written as

$$\langle n', \Gamma'| \mu_\alpha |n'', \Gamma''\rangle = \sum_{ij} \langle \tilde{\eta}^i_{n',\Gamma'}| M^{ij}_\alpha |\tilde{\eta}^j_{n'',\Gamma''}\rangle \tag{11}$$

where $M^{ij}_\alpha = \langle \Lambda_i| \mu_\alpha |\Lambda_j\rangle$ are the matrix elements of the dipole moment operator, represented in the electronic wavefunction basis set. Expanding M^{ij}_α up to first order in terms of normal

modes at R_0 we get

$$M_\alpha^{ij} = M_\alpha^{ij(0)} + \sum_k M_{\alpha,k}^{ij(1)} q_k \tag{12}$$

here $M_\alpha^{ij(0)} = (M_\alpha^{ij})_{R_0}$ is the zeroth order dipole moment contribution, $M_{\alpha,k}^{ij(1)} = \left(\frac{\partial M_\alpha^{ij}}{\partial q_k}\right)_{R_0}$ is the first order derivative, k runs through all normal mode indices.

This operator, Eq. (12), is then evaluated for transitions from the ground spin-vibronic level, 0 to other spin-vibronic levels, which requires the squares of the dipole matrix elements to the i^{th} spin-vibronic level that are given by

$$S_{f\leftarrow 0} = \sum_\alpha \left| \sum_{ij} \left(M_\alpha^{ij(0)} \langle \tilde{\eta}_{n',\Gamma'}^i | \tilde{\eta}_{n'',\Gamma''}^j \rangle + \sum_k M_{\alpha,k}^{ij(1)} \langle \tilde{\eta}_{n',\Gamma'}^i | q_k | \tilde{\eta}_{n'',\Gamma''}^j \rangle \right) \right|^2 \tag{13}$$

Finally, the relative experimental absorption intensities, $I_{f\leftarrow 0}$, are determined by the integrated cross-sections, σ_{0f}^I of the spectral lines, as in the Hitran database [47], and are related [48] to $S_{f\leftarrow 0}$ by

$$I_{f\leftarrow 0} \propto \sigma_{0f}^I \propto \nu_{0f} S_{f\leftarrow 0} \tag{14}$$

where ν_{0f} is the energy of the transition.

Evaluating the expression for $S_{f\leftarrow 0}$ requires calculating the electronic dipole moment derivatives at the CI, which was done using finite differences. It is important to note here that for each perturbed geometry, the dipole moment values calculated are in the molecule's principal axis system. However, as the molecule is perturbed, the principal axes change. The computed dipole moment for each perturbed geometry is rotated back to the principal axis system of the unperturbed geometry before dipole moment derivatives can be calculated via finite differences.

Further, dipole moment derivatives in the quasi-diabatic representation, in general, are not the same as those in the adiabatic representation. However, from the symmetry of our system it follows that for displacements along totally symmetric vibrational modes and symmetric components of doubly degenerate modes adiabatic and quasi-diabatic representations of the dipole moment operator coincide. Therefore, parameters of the dipole moment

expansion may be derived directly from the adiabatic representation.

In order to evaluate all first derivative terms in the cylindrical basis, we transform the derivatives of the dipole moment operator adiabatic matrix elements using the following relations [49]

$$\frac{\partial}{\partial q_{i,\pm}} \langle \Lambda = \pm 1 | \, \mu_{\pm} \, | \Lambda = \mp 1 \rangle = \frac{1}{\sqrt{2}} \left(\frac{\partial}{\partial q_{i,a}} \langle \Psi^{A'} | \, \mu_x \, | \Psi^{A'} \rangle - \frac{\partial}{\partial q_{i,a}} \langle \Psi^{A''} | \, \mu_x \, | \Psi^{A''} \rangle \right) \tag{15}$$

$$\frac{\partial}{\partial q_{i,\mp}} \langle \Lambda = \pm 1 | \, \mu_{\pm} \, | \Lambda = \pm 1 \rangle = \frac{1}{2\sqrt{2}} \left(\frac{\partial}{\partial q_{i,a}} \langle \Psi^{A'} | \, \mu_x \, | \Psi^{A'} \rangle + \frac{\partial}{\partial q_{i,a}} \langle \Psi^{A''} | \, \mu_x \, | \Psi^{A''} \rangle \right) \tag{16a}$$

$$\frac{\partial}{\partial q_{i,\pm}} \langle \Lambda = \pm 1 | \, \mu_{\mp} \, | \Lambda = \pm 1 \rangle = \frac{1}{2\sqrt{2}} \left(\frac{\partial}{\partial q_{i,a}} \langle \Psi^{A'} | \, \mu_x \, | \Psi^{A'} \rangle + \frac{\partial}{\partial q_{i,a}} \langle \Psi^{A''} | \, \mu_x \, | \Psi^{A''} \rangle \right) \tag{16b}$$

$$\frac{\partial}{\partial q_{i,\pm}} \langle \Lambda = \pm 1 | \, \mu_z \, | \Lambda = \mp 1 \rangle = \frac{\partial}{\partial q_{i,a}} \langle \Psi^{A'} | \, \mu_z \, | \Psi^{A'} \rangle \tag{17}$$

where $\Psi^{A'}$ and $\Psi^{A''}$ are the two components for the degenerate electronic state as represented in the abelian subgroup (C_s) of the molecular symmetry group (C_{3v}) and are related to $|\Lambda = \pm 1\rangle$ as

$$|\Lambda = \pm 1\rangle = \frac{1}{\sqrt{2}}(|\Psi^{A'}\rangle \pm i \, |\Psi^{A''}\rangle) \tag{18}$$

and $q_{i,a}$ is the totally symmetric component of the degenerate vibrational mode (q_i) in the abelian subgroup (C_s). The derivatives with respect to non-degenerate modes are given by

$$\frac{\partial}{\partial q_i} \langle \Lambda = \pm 1 | \, \mu_{\mp} \, | \Lambda = \mp 1 \rangle = \sqrt{2} \frac{\partial}{\partial q_i} \langle \Psi^{A'} | \, \mu_x \, | \Psi^{A'} \rangle = \sqrt{2} \frac{\partial}{\partial q_i} \langle \Psi^{A''} | \, \mu_x \, | \Psi^{A''} \rangle \tag{19}$$

$$\frac{\partial}{\partial q_i} \langle \Lambda = \pm 1 | \, \mu_z \, | \Lambda = \pm 1 \rangle = \frac{\partial}{\partial q_i} \langle \Psi^{A'} | \, \mu_z \, | \Psi^{A'} \rangle = \frac{\partial}{\partial q_i} \langle \Psi^{A''} | \, \mu_z \, | \Psi^{A''} \rangle \tag{20}$$

Symmetry properties of the C_{3v} group were used to simplify these equations such that they satisfy two conditions. Firstly, all off-diagonal matrix elements between $|\Psi^{A'}\rangle$ and $|\Psi^{A''}\rangle$ were eliminated and secondly, only derivatives with respect to totally symmetric

normal coordinates are present on the right hand side of eqs. (15, 16, 17, 19 and 20). Detailed symmetry relationships between the derivatives of the Cartesian dipole moment matrix elements are provided in the supplementary material.

The dipole moment derivatives were calculated at CI geometry at EOMIP-CCSDT/ANO1 level of theory using CFOUR program and are listed in Table 1 and Table 2, respectively, for the totally and non-totally symmetric modes. The values for the 0^{th} order components, $M_{\alpha}^{ij(0)}$, of the dipole expansion in Eq. (12) are 0.76194 and -0.07995 in atomic units for z and x respectively. (The value for the z component is not relevant for the spectral intensities, but is given for perspective.)

3 Experimental Data Overview

There is a great deal of experimental work on the ground electronic state of methoxy. An early work [3] on methoxy using microwave spectroscopy is a benchmark for our understanding of its rotational structure and remains the highest resolution spectrocopic work done on the molecule. However, as the study only involved the zero-point level of the ground electronic state, it is of limited value here as we need to compare our calculated results for the spin-vibronic structure of the ground state with experimentally observed structure up to more than 3000 cm^{-1} above the zero-point level.

Broad spectral coverage is provided by gas-phase-work involving laser-excited, dispersed fluorescence, which extends to spin-vibronic energies well above 3000 cm^{-1}. This work [5, 21, 7] has contributed much to our general understanding of the spin-vibronic structure of methoxy. However, due to a combination of unresolved rotational structure and insufficient experimental resolution in the dispersed fluorescence, observed transition bandwidths of $>$ 10 cm^{-1} are typically obtained. Because of the high density of spin-vibronic levels above 2000 cm^{-1}, this resolution is often insufficient to isolate and measure individual transitions with high precision. Therefore these experimental laser-excited, dispersed fluorescence measurements are of limited value for making meaningful comparisons between calculated and

experimental results.

Stimulated emission pumping (SEP) spectroscopy also uses laser excitation but rather than resolving the fluorescence stimulates the emission with another laser thereby greatly improving the experimental resolution and the spectral coverage extends to well over 3000 cm^{-1}. In some of the reported methoxy experiments [22, 23] the SEP line widths were not narrow enough to fully resolve the rotational structure.

Nonetheless, several vibronic transitions had rotationally resolved spectra and were analyzed. [15, 16, 24, 25] However, the majority of spin-vibronic bands that were used in our analysis were determined from the only SEP data available, survey spectra that were not rotationally resolved. [24] Additionally, the available data do not include transitions to all possible ground-state, spin-vibronic levels due to the selection rules for emission from the limited number of pumped vibrations of the $\tilde{A}$ electronic state. Nonetheless, the SEP work serves as very valuable experimental data and a stick diagram of the spectral results is shown as top trace of Fig. 1.

Slow-electron velocity-map imaging (SEVI) spectroscopy has also been applied [29] to methoxy with observed spin-vibronic transitions spanning the range from 0 to >2500 cm^{-1}. In these experiments the breath of the transitions was 5-10 cm^{-1}. While not quite as high a resolution as that of the SEP spectra, these data are also very valuable for comparison to the calculated structure and are shown as trace (b) of Fig. 1.

Perhaps most important, there have been direct IR absorption experiments performed on a jet cooled sample of methoxy [50, 51] and on methoxy isolated in a para-hydrogen matrix [30]. The gas phase spectrum consists of more than 1000 lines and the line widths are quite narrow, < 0.1 cm^{-1}. For some of these transitions, rotational quantum numbers can be assigned based on combination differences from the zero-point level that are well determined from the earlier microwave work. However, in only four cases could the rotational structure be successfully extrapolated to yield spin-vibronic band origins. Furthermore, even in those four cases the extrapolated origins were accurate to only about 1 cm^{-1}. However, these values agreed well with the transitions observed in the para-hydrogen matrix. For this

reason we will not discuss these gas-phase results any further, but turn to the matrix results which contain measurements of about 60 spin-vibronic energies.

The para-hydrogen matrix results are shown in trace (c) of Fig. 1. As can be seen from the figure, the matrix data is more extensive than either the SEP or SEVI results. The line widths are a few cm^{-1}, comparable to the SEP results and somewhat better than the SEVI data, although the matrix line widths broaden above 2700 cm^{-1} and become more comparable to the SEVI results. Additionally, only for the matrix spectrum are a comprehensive set of intensities for the transitions reported. For these reasons, we consider the matrix spectrum the primary experimental data to which we compare our calculated results.

Nevertheless, we have found it valuable to augment the data set for the transition energies from the para-hydrogen matrix experiments with the SEVI and SEP results. For example, the matrix spectrum does not extend to low enough energy to observe the separation between the two fine-structure components of the zero-point level, but it can be obtained from both the SEP and SEVI measurements. Likewise a line near 1100 cm^{-1} is observed by both the SEP and SEVI measurements, but not reported in the matrix. Furthermore, there are some regions of the matrix spectrum that are in part or completely obscured by precursor absorptions, e.g., the spectral region around 1600 or 1700 cm^{-1}. In this region we use the three reported SEVI transitions in place of the matrix data. A similar procedure is adopted near 2100 cm^{-1}, substituting two SEP transitions for the one very weak matrix transition reported in this spectral region. The resulting "Augmented IR (AIR) spectrum" is shown as trace (d) of Fig. 1. In this trace, we show the relative intensities for the matrix spectrum. The "augmented" line positions obtained by SEP or SEVI are shown as dashed lines and are set at half full-scale intensity for clarity. However, their intensities cannot be compared to the matrix IR ones.

Finally, it is worthwhile noting that the three experiments actually are each measuring slightly different values for the energies and none of these values are quite the same as the calculated ones. The calculation predicts the spin-vibronic eigenvalues within the ground

electronic state with respect to its lowest spin-vibronic level, the zero-point $^2E_{3/2}$, from which all observed transitions originate, and whose energy is taken as 0.

For a spectrum with rotational structure these would correspond to the origin of a given spin-vibronic transition. However, neither the SEP nor the SEVI experiments show resolved rotational structure that could be analyzed to determine the band origin. Nevertheless, the reported center of the rotational contour should be a reasonable approximation of the origin in most cases. Moreover, while for both the SEVI and SEP experiments the center of the rotational contour was reported, it would not be the same in both experiments since the rotational selection rules and hence the contours are different in the two experiments. On the other hand, the molecule is not rotating in the matrix, so its reported transition frequency would not displaced from the spin-vibronic eigenvalue. Nonetheless, even a weakly binding matrix like para-hydrogen slightly perturbs the transition energies of a molecule observed therein from those of the isolated molecule.

While all of the above effects should be considered when comparing the experimental and calculated spin-vibronic energies, none of the issues mentioned would likely cause a significant limitation in the comparison of experimental and calculated results. Empirical evidence for this statement can be found by computing (for the transitions observed in common) the root mean square deviation (RMSD) for each of the three pairs of experimental results. We find the RMSDs are as follows: RMSD(SEP-IR)= 3 cm^{-1}, RMSD(SEVI-IR)= 5 cm^{-1} and RMSD(SEP-SEVI)= 4 cm^{-1}. Reasonably, this uncertainty of 3-5 cm^{-1} would apply to comparisons between the experimental and calculated eigenenergies.

4 Spectral assignment and analysis

A goal of this work to ascertain whether it is possible is to make a line-by-line assignment of the AIR experimental lines shown in Fig. (1) to the transition frequencies calculated in the Section 2, with both sets of values being listed in Table (3). Given the line density (heterogeneous, but averaging up to one per 5 cm^{-1}), it is extremely difficult to unambiguously

assign all transitions in the methoxy spin-vibronic spectrum to above 3000 cm^{-1} based simply on absolute energy matches between the two sets. For this reason, we utilize additional information from our calculations for the analysis of the methoxy spectrum. In Section 2 the intensities of transitions from the ground spin-vibronic level to higher energy levels were also calculated. These intensities are neither measured nor calculated with the precision of the energies, but they can still be useful guides for assignments.

Besides comparing transition energies and intensities, we examine other properties that we can calculate with better confidence. Since methoxy has a total electron spin of 1/2, we expect the vibronically degenerate e levels to be split into spin-orbit doublets. These splittings can be calculated approximately from the vibronic eigenfunctions by using an extension of the Ham quenching factor (d) formulation, as described in the Supplementary Information (SI). Alternatively and more accurately, the spin-orbit coupling can be calculated variationally by adding the spin-orbit interaction to the vibronic Hamiltonian. The spin-orbit splittings computed by each of two methods are listed is Table (4). These calculated values serve to identify the spin-orbit pairs in the spectrum *via* their characteristic gaps. Once these experimental gaps are recognized, they provide nearly unique labels for the spin-orbit pairs of the degenerate vibronic levels. Fig. (S.2) shows the generally good agreement between the experimental spin-orbit gaps and those predicted by the calculations.

Once all the experimental transitions belonging to spin-orbit pairs are identified, the rest of the lines must correspond to transitions to non-degenerate a_1 and a_1 levels. Like the spin-orbit gaps these can be calculated either from the vibronic or the spin-vibronic eigenvalues and are given in Table (5) along with the corresponding experimental values. Fig. (S.3) shows a plot of the deviations between calculation and experiment. Although not quite as useful as the more numerous spin-orbit gaps, the a_1 and a_1 separations serve to identify and confirm the assignments for these remaining vibronic levels.

4.1 Adiabatic Tracking of Eigenvalues (OV)

While Tables (3-5) provide the key quantitative information to make the line assignments of the experimental transitions, it can be useful to also have a graphical presentation of this information to facilitate these assignments and also to identify various characteristics of the corresponding eigenvectors. Fig. (2) represents an example of such a presentation and it is informative to review its construction and application to assigning the spectrum.

Fig. (2) is divided into three separate parts, labeled (a)-(c). To construct part (a), we have initially neglected the spin-orbit coupling and made calculations with the potential energy matrix from Eq. (4) split into two parts

$$\mathbf{V} = \begin{pmatrix} V_{11} & 0 \\ 0 & V_{22} \end{pmatrix} + \lambda \begin{pmatrix} 0 & V_{12} \\ V_{21} & 0 \end{pmatrix} \tag{21}$$

Separating the off-diagonal and diagonal matrix elements in Eq. (21) allows us to scale the JT coupling contributions, which are all off-diagonal in the cylindrical representation, by varying in 0.1 steps the λ parameter from 0 to 1, i.e. from the no-vibronic coupling limit to that determined by fitting the quasi-diabatic analytical potential to the *ab initio* electronic surface as described in Section 2. At $\lambda = 0$, the levels are labeled by the basis functions, simple products of the doubly degenerate electronic state components and the various vibrational basis functions or modes. All these basis functions are least doubly degenerate since we are always dealing with a degenerate E electronic state. When $\lambda > 0$, the double degeneracy remains if the vibrational ket is non-degenerate. However, if the vibrational mode is doubly degenerate, the initial quadruple degeneracy is lifted giving rise to three vibronic levels of symmetry $a_1 + a_2 + e$. The avoided crossing rule is used to adiabatically track the corresponding vibronic eigenenergies based on which irreducible representation their eigenvectors transform. At $\lambda = 1$, the eigenvalues are re-labelled by the basis function(s) that has the coefficient of the largest magnitude in the vibronic eigenfunction. In Fig. (2) the label is always the same for the $\lambda = 0$ or 1 limits, but this equality does not hold for all

lines in the spectrum. Of course, the labels at the two limits must belong to basis functions of the same symmetry.

At the $\lambda = 1$ point a second calculation has been performed that includes the spin-orbit term in the Hamiltonian, which has the effect of splitting all the e vibronic states into spin-orbit pairs, which are labeled as $e_{1/2}$ and $e_{3/2}$ based on how their eigenvectors transform in the spin-double group. The spin-orbit interaction also shifts the a_1 and a_2 levels, all of which have eigenvectors that transform as $e_{1/2}$ in the spin-double group.

Part (b) of Fig. (2) corresponds to the same spin-vibronic eigenvalue spectrum in horizontal format that is presented in part (a) in vertical form. For ease of reference, levels in the two parts are connected with lines color coded according to the vibronic symmetry. The numbering, $\#n(m)$, of spin-vibronic levels and the associated lines connecting parts (a) and (b) corresponds to the experimental transition, n, (n starts from 1), shown in part (c), and the simulated line, m, where m is defined independently for $e_{3/2}$ (m starts from 0) and $e_{1/2}$ (m starts from 1) levels.

Part (c) corresponds to the experimental spectrum (see Fig. (1)) on the same horizontal axis as part (b). In parts (b) and (c) the energy levels and spectral transitions from the $e_{3/2}$ vibrationless level, have heights equivalent to their calculated and observed intensities, respectively. Matches are indicated by the black arrows between simulated and experimental spectrum lines.

4.2 Assignment of Experimental Transitions

Our assignment procedure can be illustrated by considering Fig. 2 in more detail. The first step is to use energy matching to assign the observed transitions in panel (c) to the simulated lines in panel (b). Indeed, with the spectral region depicted in Fig. 2, this step is nearly sufficient. However, in other spectral regions a given line in the simulation may plausibly be assigned to more than one spectral line or *vice versa*. To resolve the ambiguities, we consider the spectral structure caused by spin-orbit splittings between $e_{3/2}$ and $e_{1/2}$ pairs

and $e_{1/2}(a_1)$-$e_{1/2}(a_2)$ vibronic separations. For example, if a spectral line is assigned to an $e_{3/2}$ level there should be a second spectral line that is near the calculated (signed) displacement of the paired $e_{1/2}$ level, as shown in the simulated spectrum in part (b).

To help identify the displacement of the spin-orbit pair, double-headed, orange arrows (anchored at the $e_{3/2}$ component) corresponding to the *calculated* displacements are shown on the *experimental* spectral trace in panel (c) (see also Table 4). Correspondingly the calculated $e_{1/2}(a_1)$-$e_{1/2}(a_2)$ spin-vibronic energy separations are indicated on the spectrum by double-headed green arrows (anchored at the a_1 component), whose lengths are equal to the separation between two lines in the simulation (see also Table 5).

Proceeding systematically thorough Fig. 2, it first should be noticed that zero of energy in all panels corresponds to the energy of the lowest spin-vibronic level which is of $e_{3/2}$ spin-vibronic symmetry and which is the level from which all transitions originate. In panel (a) it labeled as #0(0), with the first 0 indicating it is the lowest level overall and the second 0 indicating it is also the lowest level of $e_{3/2}$ symmetry. Following this procedure we then assign the lowest excited vibrationless $e_{1/2}$ level, #1(1). The lowest spectral line corresponds to the transition between these two levels. The experimental transition is at 61.5 cm^{-1}, which matches well the predicted line at 63.5 cm^{-1}. Since all transitions originate from the same level, we label them only by their terminal level, so this transition is labelled 1 in panels (b) and (c).

The next group of vibronic levels, ν_3 and ν_6, give rise to four vibronic levels, two of which are doubly degenerate. These, in turn, give rise to six spin-vibronic levels 3_1 ($e_{1/2}$ and $e_{3/2}$), 6_1($e_{1/2}$ and $e_{3/2}$), and finally 6_1(a_1 and a_2), both $e_{1/2}$ in spin-double group symmetry. To that group of levels we assign on the basis of energy matches only, experimental lines 2-7, respectively. We assign the remaining experimental transitions, 8-13, following the same procedure. We then confirm these assignments by noting that the spin-orbit and vibronic separations closely match the assigned experimental separations. As the figure shows, there is good agreement between the predicted spin-orbit and a_1-a_1 splittings, indicated by the orange and green horizontal, double-headed arrows, respectively, and the corresponding

separations of the assigned experimental spectral lines.

Further inspection of Fig. 2 indicates that the overall deviations of spin-orbit splittings appear smaller than the deviations in absolute transition frequencies. We can confirm this statement by noting that the RMSD between calculated and observed spin-orbit gaps is 2.6 cm^{-1} (see Table 6) in this region. This can be compared to a RMSD deviation of 8.5 cm^{-1} for the matches between the experimental and calculated energies in this spectral region. Due to the low density of transitions here absolute energy matches are sufficient to make reliable assignments. Nonetheless, except for the region of the spectrum above 2400 cm^{-1} the experimental resolution is good enough to partially resolve lines separated by ≥ 2 cm^{-1}, which is comparable to the RMSD for the spin-orbit splitting predictions, but the accuracy of the predicted absolute energies is significantly poorer. Thus the calculated spin-orbit gaps, and to a lesser extent the $a_1 - a_2$ separations, serve as an extremely useful tool for confirming assignments.

Fig. (3) covers the spectral range 1600 - 2400 cm^{-1} and Fig. (4) does likewise for the 2400 - 2800 cm^{-1} range. The spectra over these two regions are similar to that in the 0-1600 cm^{-1} range with a few exceptions. As the energy increases the spectral density increases and the agreement with the theoretical calculation diminishes modestly. Nonetheless, the assignment procedure used for the 0-1600 cm^{-1} range can still be applied except that assignment ambiguities based solely on energy matches do increase, so that matches supported by line pair separations become more important.

In Fig. (3) the spin-orbit gap matches between simulation and experiment remain very good as is the lowest energy a_1-a_2 separation. However, the remaining two theoretical a_1-a_2 separations are not measured due to the fact that in each case one of the two lines is predicted to quite weak and is not observed experimentally. Accordingly the corresponding double-headed green lines in Fig. (3) are shown dashed.

Note that all predicted lines in Fig. (3) can be assigned to experimental ones. However, one experimental line, #23 at 2226.9 cm^{-1}, cannot be assigned to any theoretical line. It has been noted earlier that the matrix spectrum is partially obscured in this spectral region

by precursor or product molecules. Since neither the SEP nor the SEVI spectrum confirms this line, it is possible that the experimental line may arise from some molecule other than methoxy or perhaps an experimental artifact. Finally, it is worth mentioning that line #23 is the only example in the entire spectrum of an observed line that could not be assigned.

In Fig. (4) all predicted lines can be assigned to experimental ones. However, in several cases more than one predicted line must be assigned to the same experimental transition as the overall density of transitions increases and in particular several predicted polyads occur that are too dense to resolve experimentally. Nonetheless for the most part the combination of absolute energy matches with confirmations by predicted pair splittings allows assignment of the experimental lines with a small likelihood of error.

The final region of the experimental spectrum is shown in Fig. (5). Somewhat surprisingly the experimental spectrum is generally somewhat less dense than that of the 2400-2800 cm^{-1} range just discussed. However there are two clusters of predicted lines (see around 2830 and 2940 cm^{-1}) for which all components are assigned to an individual experimental transition. Likely this result can be laid to very close clustering of the experimental components plus the fact that the spectral resolution in this region has degraded to poorer than 5 cm^{-1} whereas lines separated by less than 2 cm^{-1} could be partially resolved in the lower energy region of the spectrum. Due to the generally lower line density many of the experimental transitions can be assigned by absolute energy matches with simulated lines, even though some of the actual deviations approach 20 cm^{-1}. Nonetheless, in almost all cases there is very good agreement between observed and calculated spin-orbit gaps and similarly for the $a_1 - a_2$ separations. The single exception is the $37e_{1/2} - 19e_{3/2}$ spin-orbit gap which is predicted to be 31.2 cm^{-1} while the measured gap is 43.5 cm^{-1}. This is the largest deviation for any spin-orbit gap in the spectrum, but no other assignment appears plausible.

5 Results and Discussion

A primary goal of this work has been to produce a true *ab initio* prediction and simulation of the vibronic energy level structure and spectrum of the methoxy radical that is sufficiently accurate to assign each experimentally observed line to a given predicted transition (or a small group of transitions predicted to lie too close to be experimentally resolved). Reference to Table 3 shows that such an assignment set has been successfully created. (Line #23 is the one possible exception to this statement, but an argument has been made earlier that it is likely an experimental artifact.) Tables (4) and (5), respectively, present the predicted and observed spin-orbit gaps and $a_1 - a_2$ separations. Table (6) shows the RMS deviations between experimentally measured energies and their predicted values for the spectral ranges, individually shown in Figs. (2)- (5), and for the global data set. Additionally, Figs. (S.1-S.3), which, respectively, graphically show the deviations for all the individual transitions, spin-orbit gaps, and $a_1 - a_2$ splittings are included in the Supplemental Information (SI).

As can be seen from Table (6) and the figures for the spectral range 0 to 2400 cm^{-1}, the RMS deviations between the predicted and observed transition energies are significantly smaller than the energy level density, so that assignments made solely on this criterion are usually unique. Nonetheless, since the RMS deviations for the spin-orbit gaps are significantly smaller, these matches provide an excellent confirmation of the assignments. However, for the two spectral ranges above 2400 cm^{-1} the density of energy levels and so spectral transitions increases dramatically as do the RMS deviations between simulated and experimental line positions. This results in a situation where multiple assignments become plausible if they are based solely on absolute energies. Therefore, the significantly smaller deviations for spin-orbit gaps and $a_1 - a_2$ splittings become crucial for unique, credible assignments in this spectral region.

Once the credibility of the assignments has been established, it is possible to use them to gain further insight into the spectrum. For example, there has long been keen interest in the part of the spectrum displayed in Fig. (5). It is expected to contain the symmetric (1^1)

and asymmetric (4^1) C-H stretch fundamentals, which have not previously been assigned experimentally. From Fig. (5) it is clear that transitions #45 and #46 are assigned as the spin-orbit pair of the 1^1 fundamental and, for easy reference, are marked with green asterisks in the figure. (It should, of course, be noted that an assignment of 1^1 to any particular experimental level is an approximation implying only that the assigned eigenvalue adiabatically correlates with 1^1 at $\lambda = 0$ or the 1^1 basis function has one of the largest coefficients in the assigned level's eigenfunction and hence possesses some of its expected properties. Indeed reference to Fig. (5) in the text and Table S.2 in the SI shows that for the assigned lines both conditions are satisfied.)

The 4^1 fundamental has four vibronic components. Transitions #46 and #52 are assigned (in the same sense as the 1^1 assignments in that these levels adiabatically correlate to 4^1 at$\lambda = 0$ and the 4^1 basis function possesses the largest coefficient in each assigned level's eigenfunction expansion) to the non-degenerate a_1 and a_2 vibronic components, respectively, which are marked with black asterisks. Finally, transitions #48 and #50 (marked with red asterisks in Fig. (5)) are assigned to the 4^1 spin-vibronic pair of states, $e_{1/2}$ and $e_{3/2}$, respectively, that arise from the degenerate 4^1 e level. (However, while these levels do adiabatically correlate with 4^1, at the $\lambda = 1$ diabatic limit the overtone of the O-C-H bending mode, 2^2, has the largest coefficient in the eigenvector expansion, but 4^1 has the next largest coefficient.)

In addition to assigning the observed spectral transitions based on the overall energies (as well as the spin orbit and $a_1 - a_2$ splittings) we can also use the line intensity information for that purpose. In Section 2 we presented the equations that calculate the experimentally observed cross sections and these results are presented in Table 1, which we discuss in more detail below.

However, first we consider how intensity information supports the assignments of the ν_1 and ν_2 fundamentals. The discussion also demonstrates the limitations of such assignments given the extensive mixing of the basis functions in the molecule's spin-vibronic eigenfunctions. Eq. (12) in Section 2 shows that each component (z and $\pm$ in cylindrical coordinates)

of the transition dipole has contributions from the derivatives of the dipole moment along each normal coordinate as well as a contribution from the dipole transition moment between the two electronic components ($\Lambda = \pm 1$) of the basis set.

As shown in Section 2 of the SI, the three cylindrical components of the dipole moment have strict selection rules for transitions from the $e_{3/2}$ zero-point level. Only the μ_z component can drive transitions to excited $e_{3/2}$ states while only the $\mu_\pm$ components drive transitions to $e_{1/2}$ levels. In the absence of spin-orbit coupling the latter selection rule becomes even more selective in that μ_- only drives transitions to nondegenerate basis functions, a_1 and a_2, while μ_+ only drives transitions to the $e_{1/2}$ components of spin-orbit doublets.

Eq. (12) shows that the net transition moment is the algebraic sum of seven components, six of which each contain the dipole derivative with respect to a given normal coordinate. These are the usual transition moments that drive vibrational transitions for each of the normal modes in a molecule with nondegenerate electronic states. When degenerate electronic states occur, the $\mu_\pm$ component of the dipole moment *and* its derivatives drive transitions between the components of the electronic states.

If the molecule's eigenfunctions correspond to those of the basis set, then the assignment of a given transition to a single mode would be rigorous, since for only one q_m value would the matrix element of the dipole moment not vanish. Of course this is not the case for methoxy. However if a single q_m term dominates the sum, assigning the transition to that single mode may still be appropriate for methoxy.

It is therefore reasonable to consider the individual terms in the sum over the modes in Eq. (13). In the SI we detail how to accomplish this sum and present a plot, Fig. (S.5), showing the q_m comtribution for each transition in the observed spectral range. In Fig. (6) we have enlarged this plot for the spectral region shown in Fig. (5). Using these results, we can obtain an additional (somewhat less precise) criterion for a given assignment besides our previous two: absolute energy and separation energy (spin orbit or $a_1 - a_2$ splitting) from another relatively nearby spectral line.

To illustrate the usefulness of this approach, we can apply our third criterion to the ν_1 and ν_4 assignments that we have previously made. Experimental lines, #45 and #46, are assigned to the simulated transitions to the $19e_{3/2}$ and $37e_{1/2}$ spin orbit pair of ν_1. As the top trace of Fig. (6) shows, the dipole derivative with respect to q_1 is clearly the most dominant contribution to the $19e_{3/2}$ transition; moreover, it is the only the transition with a significant contribution from ν_1 in this spectral region.

The situation is somewhat more complex for line #46 assigned to the $37e_{1/2}$ in the simulation. The middle trace of Fig. (6) shows that the $37e_{1/2}$ transition has ν_4 as the leading contribution, but ν_1 has the next largest contribution. It also shows that a significant magnitude of the ν_1 transition moment has been borrowed by simulated transitions $39e_{1/2}$, $40e_{1/2}$ and $44e_{1/2}$. Thus, one could reasonably argue that the contribution of ν_1 to the transition moment of $37e_{1/2}$ is consistent with, but not by itself compelling evidence, for assigning this transition to ν_1 $e_{1/2}$. However, taken with the two more precise energy criteria, this assignment is quite reasonable.

The situation is similar with the spin orbit pair, experimental lines #48 and #50, that are assigned, respectively, to the $40e_{1/2}$ and $21e_{3/2}$ simulated transitions that are correlated with ν_4. As Fig. (6) shows, by far the largest contribution to the $21e_{3/2}$ transition dipole is from ν_4. Likewise, the largest contribution to $40e_{1/2}$ is from ν_4.

Experimental lines #45 and #52 are assigned to transitions to the nondegenerate simulated levels $38e_{1/2}$ and $45e_{1/2}$, respectively. Reference to Fig. (6) shows that in the case of $38e_{1/2}$ only the contribution from ν_4 is large enough to show in the figure. For $45e_{1/2}$, the q_4 dipole is clearly the largest contribution. However, it should be noted that $41e_{1/2}$, $42e_{1/2}$, and $43e_{1/2}$ also have some comparable contributions from the q_4 dipole. However, the $45e_{1/2}$ assignment is most consistent with the predicted $a_1 - a_2$ energy splitting.

The conclusions described above for the ν_1 and ν_4 spin vibronic fundamentals are representative of most of the assignments of the lines elsewhere in the spectrum. However, there are a few cases where basis function mixing in the eigenfunctions is so extensive that no single basis function label is physically reasonable. It is also worth stressing that, as

with the above example of ν_1 and ν_4, in no case is a single basis function label for the true eigenfunction quantitatively rigorous.

We now turn to a comparison of the simulated intensities and compare them to the values obtained from the matrix IR absorption spectrum of methoxy[30]. Both the simulated and experimental numerical values are listed in Table (3) and all the simulated values are shown in Figs. (2)- (5). All the intensities are relative and both simulated and experimental values have been adjusted to the 13.0 km/mol value for the $3e_{1/2}$ transition predicted by reference [30]. Additionally, a plot (see Fig. S4) of the deviations between the two values *vs* transition energy is given in the SI. The observed experimental lines have a dynamic range of about 250 (0.1 to 25 on the assigned scale). As Fig. S4 shows, there are a pair of experimental transitions (lines #7 and #9) that are several times stronger than predicted and another set (lines #49, #50, and #51) that is similarly much stronger than predicted. These lines are considered outliers. If the outliers are excluded, then the RMSD between simulated and observed intensities is close to 2.0 km/mol, which is not necessarily inconsistent with the ability of theory to predict intensity , particularly as exacerbated by the difficulty inherent in describing a JT system. However, the simulations are still helpful for assignment purposes as their intensities can be divided into three categories: weak, medium and strong transitions. We find that the predicted and observed categories have a strong correlation for the assigned lines.

At this point there is no obvious reason why the intensity predictions are not somewhat more quantitative, especially for the outliers. Of course, one could consider higher order expansions of the dipole operator. However, previous calculations of Nagesh and Sibert [37] indicate that the contributions of such terms are small. Additionally, we have calculated some sample quadratic terms and reach similar conclusions. We have noted that our present results bear a relatively strong resemblance to the results obtained by Lee, *et. al.*[30]. Both predictions have the same five outliers and for the rest of the transitions the previous predictions show a very similar RMSD of 2.1 km/mol. Since the two calculations are very different in detail, this is an argument for the creditability of both calculations.

Spectroscopic intensity measurements are always much less reliable than transition energy measurements, but one would typically expect accuracy approaching 25% or so for completely resolved, relatively strong lines. However, only a few of the reported lines fit that criterion. For the most part the observed lines actually contain from two to seven partially resolved or unresolved transitions. Since the reported values are integrated intensities, spectral fitting of the composite lines is required, which involves variations of numerous parameters, i.e. different widths and intensities for each line and the separations between them. This process could lead to errors of up to a factor of two for the integrated contours, comparable to the RMSD between observed and predicted values. Only for the outlier lines is the expected discrepancy between experimental and predicted line intensities clearly inconsistent with that shown in Table (3). Perhaps the higher energy outliers could be explained by an underlying strong, broad absorption. However, the spectrum in the region where the lower energy outlier pair lie is not consistent with such an explanation, but one cannot rule out chance overlap between these two bands and some relatively sharp absorptions due another molecule in the matrix. A further investigation of the intensity disagreement, especially for the outliers, is warranted.

6 Conclusions

The analysis of the spectral data across various ranges demonstrates a robust correlation between experimental observations and our completely *ab initio* predictions, especially with respect to the spin-orbit gaps and $a_1 - a_2$ separations. While deviations in absolute transition energies are larger, the consistency of spin-orbit splitting predictions in particular serves as a critical tool for confirming spectral assignments. This is to be expected as the ultimate limitation to the *ab initio* prediction is presumably the computed potential, which directly affects the absolute line positions, but which less directly affects the spin-orbit splittings. The spectral region from zero to more than 3000 cm^{-1} reveals a generally effective assignment process, despite increasing complexities and ambiguities due to the higher

density of transitions. Notably, the final spectral region from 2800 to 3000 cm^{-1} offers promising new insights, including presumptive assignments for the previously unassigned C-H stretch fundamentals. Future work could include rotational-fine structure analysis as an independent method to confirm vibronic state assignments by characterizing the symmetry of the observed states. Overall, the findings underscore the value of theoretical calculations in guiding experimental analysis and enhancing our understanding of molecular spectral features.

7 Supplementary Material

The PES for Methoxy and other theoretical and computational details for the results can be found in the supplementary material published online with this paper.

Acknowledgement

The authors gratefully acknowledge very useful discussions with Y. P. Lee concerning the experimental details of the methoxy spectra taken in a para-hydrogen matrix. K.S. and J.F.S. acknowledge the financial support received from the U.S. Department of Energy, Office of Basic Energy Sciences under Award DE-SC0018164. O.A.V. gratefully acknowledges a Terry A. Miller Postdoctoral Fellowship from the Ohio State University. T.A.M. acknowledges support from the Ohio Supercomputer via Project No. PAS0540.

Data availability statement

The data that support the findings of this study are available within the article and its supporting information. The data that support the findings of this study are available from the corresponding author upon request.

References

[1] K. L. Demerjian, Adv. Environ. Sci. Technol. **4**, 1–262 (1974).

[2] W. A. Glasson, Environmental Science & Technology **9**, 1048–1053 (1975).

[3] Y. Endo, S. Saito, and E. Hirota, J. Chem. Phys. **81**, 122 (1984).

[4] T. Barckholtz and T. A. Miller, Int'l. Rev. of Phys. Chem. **17**, 435 (1998).

[5] S. C. Foster, P. Misra, T. Y. D. Lin, C. P. Damo, C. C. Carter, and T. A. Miller, J. Phys. Chem. **92**, 5914 (1988).

[6] G. Inoue, H. Akimoto, and M. Okuda, Chem. Phys. Lett. **63**, 213 (1979).

[7] Y.-Y. Lee, G.-H. Wann, and Y.-P. Lee, J. Chem. Phys. **99**, 9465–9471 (1993).

[8] M. J. Nee, A. Osterwalder, J. Zhou, and D. M. Neumark, J. Chem. Phys. **125**, 014306/1–014306/9 (2006).

[9] T. M. Ramond, G. E. Davico, R. L. Schwartz, and W. C. Lineberger, J. Chem. Phys. **112**, 1158 (2000).

[10] C. L. Osborn, D. J. Leahy, E. M. Ross, and D. M. Neumark, Chem. Phys. Lett. **235**, 484 (1995).

[11] D. L. Osborn, D. J. Leahy, and D. M. Neumark, J. Chem. Phys. A **101**, 6583 (1997).

[12] H. E. Radford and D. K. Russell, J. Chem. Phys. **66**, 2222 (1977).

[13] T. Momose, Y. Endo, E. Hirota, and T. Shida, J. Chem. Phys. **88**, 5338 (1988).

[14] T. Momose, Y. Endo, E. Hirota, and T. Shida, J. Chem. Phys. **90**, 4636 (1989).

[15] J. Liu, M.-W. Chen, D. Melnik, J. T. Yi, and T. A. Miller, J. Chem. Phys. **130**, 074302 (2009).

[16] J. Liu, M.-W. Chen, D. Melnik, T. A. Miller, Y. Endo, and E. Hirota, J. Chem. Phys. **130**, 074303 (2009).

[17] D. Melnik, J. Liu, M.-W. Chen, and T. A. Miller, J. Chem. Phys. **135**, 094310 (2011).

[18] B. E. Applegate, M. B. Pushkarsky, and T. A. Miller, J. Phys. Chem. **103**, 1538 (1999).

[19] D. K. Russell and H. E. Radford, J. Chem. Phys. **72**, 2750 (1980).

[20] K. Sharma, T. A. Miller, and J. F. Stanton, Int. Rev. Phys. Chem. **40**, 165–298 (2021).

[21] P. Misra, X. Zhu, and C. Hsueh, Chem. Phys. **178**, 377 (1993).

[22] A. Geers, J. Kappert, F. Temps, and J. W. Wiebrecht, J. Chem. Phys. **93**, 1472 (1990).

[23] A. Geers, J. Kappert, F. Temps, and J. W. Wiebrecht, J. Opt. Soc. Am. B **7**, 1935 (1990).

[24] F. Temps, Adv. Series Phys. Chem. **4**, 375 (1995).

[25] A. Geers, J. Kappert, F. Temps, and T. J. Sears, J. Chem. Phys. **98**, 4297 (1993).

[26] S. Dertinger, A. Geers, J. Kappert, J. Wiebrecht, and F. Temps, Faraday Discuss. **101**, 3618 (1994).

[27] A. Geers, J. Kappert, F. Temps, and J. Wiebrecht, J. Chem. Phys. **101**, 3618 (1994).

[28] A. G. J. Kappert, F. Temps, and J. Wiebrecht, J. Chem. Phys. **101**, 3634 (1994).

[29] M. L. Weichman, L. Cheng, J. B. Kim, J. F. Stanton, and D. M. Neumark, J. Chem. Phys. **146**, 224309 (2017).

[30] Y.-F. Lee, W.-T. Chou, B. A. Johnson, D. P. Tabor, E. L. Sibert, and Y.-P. Lee, J. Mol. Spectros. **310**, 57–67 (2015).

[31] J. Schmidt-Klugmann, H. Koppel, S. Schmatz, and P. Botschwina, Chem. Phys. Lett. **369**, 21–30 (2003).

[32] A. V. Marenich and J. E. Boggs, J. Chem. Phys. **119**, 3098–3105 (2003).

[33] A. V. Marenich and J. E. Boggs, J. Chem. Phys. **122**, 024308/1–024308/11 (2005).

[34] A. V. Marenich and J. E. Boggs, Inter. J. Quant. Chem. **106**, 2609–2616 (2006).

[35] A. V. Marenich and J. E. Boggs, J. Mol. Struct. **780-781**, 163–170 (2006).

[36] J. Nagesh and E. L. Sibert, Phys. Chem. Chem. Phys. **12**, 8250 (2010).

[37] J. Nagesh and E. L. Sibert, J. Phys. Chem. **116**, 3846–3855 (2012).

[38] J. Nagesh, E. L. Sibert, and J. F. Stanton, Spectro. Acta Part A **119**, 90–99 (2014).

[39] T. Zeng and I. Seidu, Phys. Chem. Chem. Phys. **19**, 11098–11110 (2017).

[40] J. Brown, R. A. Lang, and T. Zeng, J. Chem. Theory Comput. **17**, PMID: 34110818, 4392–4402 (2021).

[41] E. Pradhan and T. Zeng, J. Chem. Theory Comput. **19**, PMID: 37847554, 7776–7786 (2023).

[42] K. Sharma, O. A. Vasilyev, T. A. Miller, and J. F. Stanton, Journal of Physics: Conference Series **2769**, 012002 (2024).

[43] K. Sharma, S. Garner, T. A. Miller, and J. F. Stanton, J. Phys. Chem. A **123**, 4990–5004 (2019).

[44] J. Watson, J. Mol. Spectrosc. **50**, 281 (1974).

[45] X. Liu, L. Yu, and T. A. Miller, J. Mol. Spectrosc. **140**, 112 (1990).

[46] P. R. Bunker and P. Jensen, *Molecular symmetry and spectroscopy* (National Research Council Canada, 2006).

[47] L. S. Rothman et al., J. Quant. Spectrosc. Radiat. Transfer **96**, 139 (2005).

[48] P. F. Bernath, *Spectra of atoms and molecules*, Second Edition (Oxford University Press, New York, NY, 2005).

[49] M. S. Child and H. C. Longuet-Higgins, Phil. Tran. Roy. Soc. Lond. Series A, Math. and Phys. Sci. **254**, 259 (1961).

[50] J.-x. Han, Y. G. Utkin, H.-b. Chen, L. A. Burns, and R. F. Curl, The Journal of Chemical Physics **117**, 6538–6545 (2002).

[51] J. Han, S. Hu, H. Chen, Y. Utkin, J. M. Brown, and R. F. Curl, Phys. Chem. Chem. Phys. **9**, 3725 (2007).

Table 1: Derivatives of dipole moment (a.u.) for the totally symmetric modes as determined from the CH_3O potential fitted to the EOM-CCSDT/ANO1 data.

Mode	Cartessian Derivatives			Cylindrical Derivatives	
	$\langle A'\|\frac{\partial\mu_x}{\partial q_{ia}}\|A'\rangle$	$\langle A''\|\frac{\partial\mu_x}{\partial q_{ia}}\|A''\rangle$	$\langle A'\|\frac{\partial\mu_z}{\partial q_i}\|A'\rangle$	$\langle \Lambda=\pm1\|\frac{\partial\mu_\mp}{\partial q_i}\|\Lambda=\mp1\rangle$	$\langle \Lambda=\pm1\|\frac{\partial\mu_z}{\partial q_i}\|\Lambda=\pm1\rangle$
ν_1	-0.01205	0.01205	0.01811	-0.01704	0.01811
ν_2	-0.00519	0.00519	-0.01248	-0.00733	-0.01248
ν_3	0.01622	-0.01622	-0.03255	0.02294	-0.03255

Table 2: Derivatives of dipole moment (a.u.) for the non-totally symmetric modes as determined from the CH_3O potential fitted to the EOM-CCSDT/ANO1 data.

	Cartessian Derivatives			Cylindrical Derivatives		
Mode	$\langle A'\|\frac{\partial\mu_x}{\partial q_{ia}}\|A'\rangle$	$\langle A''\|\frac{\partial\mu_x}{\partial q_{ia}}\|A''\rangle$	$\langle A'\|\frac{\partial\mu_z}{\partial q_{ia}}\|A'\rangle$	$\frac{\langle \Lambda=\pm1\|\frac{\partial\mu_\mp}{\partial q_{i\pm}}\|\Lambda=\pm1\rangle}{\langle \Lambda=\pm1\|\frac{\partial\mu_\pm}{\partial q_{i\mp}}\|\Lambda=\pm1\rangle}$	$\langle \Lambda=\pm1\|\frac{\partial\mu_\pm}{\partial q_{i\mp}\|\Lambda=\mp1}\rangle$	$\langle \Lambda=\pm1\|\frac{\partial\mu_z}{\partial q_{i\pm}}\|\Lambda=\pm1\rangle$
ν_4	0.01814	0.03913	-0.02344	0.02025	-0.01484	-0.02344
ν_5	-0.02263	-0.02479	-0.02622	-0.01677	0.00153	-0.02622
ν_6	-0.01283	-0.00269	0.00233	-0.00549	-0.00717	0.00233

Table 3: Comparison of Simulated and Experimental Transition Energies (cm^{-1}) (AIR spectrum) and Intensities (Methoxy IR absorption spectrum). Spin-vibronic transitions in the simulation have been assigned using two labeling schemes: adiabatic tracking and spin-vibronic eigenvector analysis. See Section 4 for details.

	Simulation				Experiment		
# Symmetry	Adiabatic assignment	Eigenvector assignment	Energy	Intensity	# Line	AIR Energy	Intensity
$0e_{3/2}$	0^0	0^0	0.0		0	0.0	
$1e_{1/2}$	0^0	0^0	63.5	3.796	1	61.5	[a]
$2e_{1/2}$	6^1	6^1	682.5	5.852	2	689.3	7.1
$3e_{1/2}$	6^1	6^1	949.0	13.00	3	945.9	13.0
$1e_{3/2}$	3^1	3^1	1045.5	9.682	4	1041.8	2.4
$4e_{1/2}$	3^1	3^1	1110.1	6.177	5	1108.0	[a]
$5e_{1/2}$	6^1	$5^1;6^1$	1237.4	7.686	6	1224.6	12.1
$2e_{3/2}$	6^1	$6^1;6^2$	1245.0	3.679	7	1233.7	20.2
$6e_{1/2}$	5^1	5^1	1348.3	3.578	8	1346.8	5.4
$3e_{3/2}$	2^1	2^1	1362.6	2.908	9	1365.7	27.5
$7e_{1/2}$	2^1	2^1	1403.3	1.063	10	1411.3	0.1
$8e_{1/2}$	5^1	5^1	1439.8	1.370	11	1427.2	3.9
$9e_{1/2}$	5^1	$2^1;5^1$	1505.6	1.021	12	1519.9	3.5
$4e_{3/2}$	5^1	5^1	1509.9	1.434	13	1523.0	7.7
$10e_{1/2}$	3^2	6^2	1633.8	0.118	14	1638.0	[a]
$5e_{3/2}$	3^2	6^2	1678.1	0.002	15	1677.0	[a]
$11e_{1/2}$	3^16^1	3^16^1	1747.1	1.723	16	1741.0	[a]
$12e_{1/2}$	3^16^1	5^16^1	2003.8	1.038 (3.43)	17	1995.9	3.9
$6e_{3/2}$	3^16^1	5^16^1	2004.4	2.388 (3.43)	17	1995.9	3.9
$13e_{1/2}$	3^16^1	3^16^1	2009.5	1.494	18	2000.6	3.6
$14e_{1/2}$	6^2	2^16^1	2053.6	0.785	19	2069.0	0.1
$7e_{3/2}$	6^2	3^2	2075.9	0.010	19	2069.0	0.1
$15e_{1/2}$	6^2	3^2	2133.4	1.623	20	2132.0	[a]
$16e_{1/2}$	2^16^1	6^3	2186.7	0.472	21	2191.4	1.1
$17e_{1/2}$	6^2	$3^2;6^1;6^3$	2215.9	7.550	22	2217.7	1.1
—	—	—	—	—	23	2226.9	2.3
$8e_{3/2}$	6^2	$6^1;3^16^1;3^16^2$	2239.8	0.077	24	2242.1	1.6
$18e_{1/2}$	2^13^1	5^16^1	2294.6	0.459	25	2286.1	1.7
$9e_{3/2}$	2^13^1	5^16^1	2294.8	0.440	26	2291.5	1.5
$19e_{1/2}$	6^2	2^16^1	2311.0	0.019	—	—	—
$20e_{1/2}$	2^16^1	3^15^1	2344.3	3.742	27	2357.2	4.2
$10e_{3/2}$	2^16^1	2^13^1	2359.1	0.038	28	2365.5	0.4
$21e_{1/2}$	2^16^1	3^15^1	2386.3	0.044	—	—	—
$11e_{3/2}$	3^15^1	$2^13^1;3^16^2$	2442.8	0.375	29	2454.3	1.3
$22e_{1/2}$	3^15^1	$2^13^1;3^16^2$	2468.5	0.220	30	2474.6	1.5
$23e_{1/2}$	3^15^1	3^15^1	2475.8	1.224	31	2482.2	1.9
$24e_{1/2}$	3^15^1	$3^15^1;6^3$	2491.9	2.380	32	2497.8	0.4
$12e_{3/2}$	5^16^1	6^3	2514.0	0.092	33	2511.7	2.6
$25e_{1/2}$	5^16^1	2^13^1	2522.6	0.394	34	2522.7	1.2
$13e_{3/2}$	5^16^1	6^3	2528.2	0.655	35	2532.6	1.1
$26e_{1/2}$	5^16^1	5^16^2	2541.7	0.855	36	2541.9	3.3
$27e_{1/2}$	5^16^1	6^3	2556.3	1.682	37	2552.1	1.6
$28e_{1/2}$	5^16^1	$2^15^1;2^16^1;3^15^1$	2565.4	0.019 (0.19)	38	2565.4	3.6
$14e_{3/2}$	5^16^1	3^15^1	2565.5	0.171 (0.19)	38	2565.4	3.6
$29e_{1/2}$	2^2	$5^16^1;5^16^2;5^2$	2585.7	0.388	39	2584.6	3.0
$15e_{3/2}$	2^2	5^2	2663.1	0.578 (0.95)	40	2651.1	0.8

[a] no intensity data available

Table 3: (*Continued*)

	Simulation				Experiment		
# Symmetry	Adiabatic assignment	Eigenvector assignment	Energy	Intensity	# Line	AIR Energy	Intensity
$30e_{1/2}$	$2^1 5^1$	$2^1 5^1; 5^1 6^1; 5^1 6^2$	2665.3	0.373 (0.95)	40	2651.1	0.8
$31e_{1/2}$	$2^1 5^1$	$2^1 5^1$	2688.0	0.096 (0.34)	41	2713.8	0.6
$32e_{1/2}$	$2^1 5^1$	$3^1 6^2$	2691.2	0.039 (0.34)	41	2713.8	0.6
$16e_{3/2}$	5^2	2^2	2695.0	0.202 (0.34)	41	2713.8	0.6
$33e_{1/2}$	5^2	5^2	2704.0	0.059	42	2732.2	0.4
$17e_{3/2}$	5^2	$3^1 6^2$	2739.5	0.003 (0.33)	43	2773.1	1.6
$34e_{1/2}$	5^2	5^2	2743.5	0.329 (0.33)	43	2773.1	1.6
$18e_{3/2}$	$2^1 5^1$	5^2	2764.3	0.958 (2.83)	44	2788.7	3.4
$35e_{1/2}$	5^2	$2^1 5^1$	2768.0	1.868 (2.83)	44	2788.7	3.4
$36e_{1/2}$	1^1	$3^2 6^1$	2793.5	0.140 (2.69)	45	2804.5	6.1
$19e_{3/2}$	4^1	1^1	2799.5	2.550 (2.69)	45	2804.5	6.1
$20e_{3/2}$	1^1	$2^2; 5^2$	2828.7	0.010 (23.57)	46	2848.0	*a*
$37e_{1/2}$	4^1	$1^1; 4^1$	2830.7	11.418 (23.57)	46	2848.0	*a*
$38e_{1/2}$	4^1	4^1	2834.8	12.143 (23.57)	46	2848.0	*a*
$39e_{1/2}$	$3^2 6^1$	$2^2; 5^2$	2850.3	1.741	47	2866.5	3.4
$40e_{1/2}$	5^2	4^1	2891.0	2.804	48	2887.5	7.6
$41e_{1/2}$	$3^2 6^1$	5^2	2895.0	0.000	—	—	—
$42e_{1/2}$	$3^2 6^1$	$5^2; 5^1 6^2$	2908.6	0.306	49	2901.3	15.7
$21e_{3/2}$	3^3	$4^1; 2^1 5^1$	2923.3	2.847	50	2917.4	25.3
$22e_{3/2}$	$3^1 6^2$	4^1	2939.6	6.499 (7.14)	51	2940.5	26.4
$43e_{1/2}$	3^3	$5^1 6^2$	2940.9	0.472 (7.14)	51	2940.5	26.4
$44e_{1/2}$	4^1	$2^1 5^1; 2^2$	2941.8	0.172 (7.14)	51	2940.5	26.4
$45e_{1/2}$	$3^1 6^2$	4^1	2950.4	0.403	52	2967.0	6.7
$23e_{3/2}$	$3^1 6^2$	$5^1 6^2$	2965.3	2.510	53	2982.2	7.8
$46e_{1/2}$	$3^2 6^1$	$2^1 6^2$	2996.4	0.673	54	3010.9	1.6
$47e_{1/2}$	$3^2 6^1$	$5^1 6^2$	3001.3	0.008	55	3020.2	2.3
$48e_{1/2}$	$3^1 6^2$	$5^1 6^2; 5^1 6^3$	3020.8	0.002	—	—	—
$24e_{3/2}$	$3^1 6^2$	$2^1 6^2$	3037.2	0.129	56	3052.7	0.4
$49e_{1/2}$	$3^1 6^2$	$3^2 6^1$	3058.4	0.015	57	3062.2	1.6

[a] no intensity data available

Table 4: Methoxy spin-orbit gaps in e vibronic states (cm^{-1}) determined from spin-orbit quenching factors, d, differences in the variationally computed eigenvalues Eq. (4), and values determined from experimental transition frequencies.

Quenching factor calculation				Variational calculation		Experiment	
Level	Energy	d	Gap	Levels	Gap	Lines	Gap
$0e$	0.0	0.478	63.6	$1e_{1/2}$–$0e_{3/2}$	63.5	1–0	61.5
$1e$	1045.8	0.486	64.6	$4e_{1/2}$–$1e_{3/2}$	64.6	5–4	66.2
$2e$	1210.9	0.056	7.4	$2e_{3/2}$–$5e_{1/2}$	7.6	7–6	9.1
$3e$	1352.7	0.308	41.0	$7e_{1/2}$–$3e_{3/2}$	40.7	10–9	45.6
$4e$	1471.9	0.036	4.8	$4e_{3/2}$–$9e_{1/2}$	4.3	13–12	3.1
$5e$	1623.4	0.334	44.4	$5e_{3/2}$–$10e_{1/2}$	44.3	15–14	39.0
$6e$	1973.6	0.005	0.7	$6e_{3/2}$–$12e_{1/2}$	0.6	17–17	0.0
$7e$	2073.3	0.437	58.1	$15e_{1/2}$–$7e_{3/2}$	57.5	20–19	63.0
$8e$	2194.9	0.185	24.6	$17e_{1/2}$–$8e_{3/2}$	23.9	24–22	24.4
$9e$	2261.6	0.002	0.2	$9e_{3/2}$–$18e_{1/2}$	0.2	26–25	5.4
$10e$	2322.7	0.124	16.5	$10e_{3/2}$–$20e_{1/2}$	14.8	28–27	8.3
$11e$	2423.7	0.211	28.0	$22e_{1/2}$–$11e_{3/2}$	25.7	30–29	20.3
$12e$	2485.5	0.031	4.1	$25e_{1/2}$–$12e_{3/2}$	8.6	34–33	11.0
$13e$	2507.0	0.239	31.8	$27e_{1/2}$–$13e_{3/2}$	28.1	37–35	19.5
$14e$	2532.5	0.001	0.1	$14e_{3/2}$–$28e_{1/2}$	0.1	38–38	0.0
$15e$	2636.5	0.010	1.4	$30e_{1/2}$–$15e_{3/2}$	2.2	40–40	0.0
$16e$	2670.4	0.032	4.2	$16e_{3/2}$–$32e_{1/2}$	3.8	41–41	0.0
$17e$	2685.6	0.287	38.2	$17e_{3/2}$–$33e_{1/2}$	35.5	43–42	40.9
$18e$	2716.6	0.205	27.2	$18e_{3/2}$–$34e_{1/2}$	20.8	44–43	15.6
$19e$	2786.8	0.249	33.2	$37e_{1/2}$–$19e_{3/2}$	31.2	46–45	43.5
$20e$	2804.5	0.187	24.8	$39e_{1/2}$–$20e_{3/2}$	21.6	47–46	18.5
$21e$	2873.8	0.293	39.0	$21e_{3/2}$–$40e_{1/2}$	32.3	50–48	29.9
$22e$	2904.6	0.034	4.5	$44e_{1/2}$–$22e_{3/2}$	2.2	51–51	0.0
$23e$	2949.6	0.276	36.7	$47e_{1/2}$–$23e_{3/2}$	36.0	54–52	43.9
$24e$	2984.6	0.309	41.2	$24e_{3/2}$–$46e_{1/2}$	40.8	–	–

Table 5: The a_1-a_2 vibronic energy level gaps (cm^{-1}), differences in the variationally computed $e_{1/2}$-$e_{1/2}$ eigenvalues of the spin-vibronic Hamiltonian (4), and values determined from experimental transition frequencies.

Vibronic		Spin-vibronic		Experiment	
Levels	Gap	Levels	Gap	Levels	Gap
$1a_2$-$1a_1$	262.5	$3e_{1/2}$-$2e_{1/2}$	266.5	3-2	256.6
$2a_1$-$2a_2$	69.3	$8e_{1/2}$-$6e_{1/2}$	91.5	11-8	80.4
$3a_2$-$3a_1$	257.9	$13e_{1/2}$-$11e_{1/2}$	262.4	18-16	259.6
$4a_2$-$4a_1$	253.6	$19e_{1/2}$-$14e_{1/2}$	257.4	–	–
$5a_1$-$5a_2$	210.0	$21e_{1/2}$-$16e_{1/2}$	199.6	–	–
$6a_2$-$6a_1$	22.2	$24e_{1/2}$-$23e_{1/2}$	16.1	32-31	15.6
$7a_1$-$7a_2$	45.2	$29e_{1/2}$-$26e_{1/2}$	44.0	39-36	42.7
$8a_1$-$8a_2$	69.5	$35e_{1/2}$-$31e_{1/2}$	80.0	44-41	74.9
$9a_2$-$9a_1$	96.4	$41e_{1/2}$-$36e_{1/2}$	101.5	–	–
$10a_2$-$10a_1$	98.6	$45e_{1/2}$-$38e_{1/2}$	115.6	52-46	119.0
$11a_2$-$11a_1$	102.5	$48e_{1/2}$-$42e_{1/2}$	112.2	(55-49)	(118.9)
$12a_2$-$12a_1$	110.1	$49e_{1/2}$-$43e_{1/2}$	117.5	56-51	112.2

Table 6: RMS Deviations between Simulated and Experimental Transition Energies, Spin-orbit Gaps, and $e_{1/2}(a_1)$-$e_{1/2}(a_2)$ Separations for Various Spectral Regions.

Region, cm^{-1}	RMSD		
	Frequencies	SO gaps	$e_{1/2}(a_1)$-$e_{1/2}(a_2)$ sep.
0-1600	8.5	2.6	12.7
1600-2400	7.4	4.6	7.8
2400-2800	16.5	3.7	3.1
2800-3062	12.3	6.9	4.5
0-3062	12.4	4.4	6.1

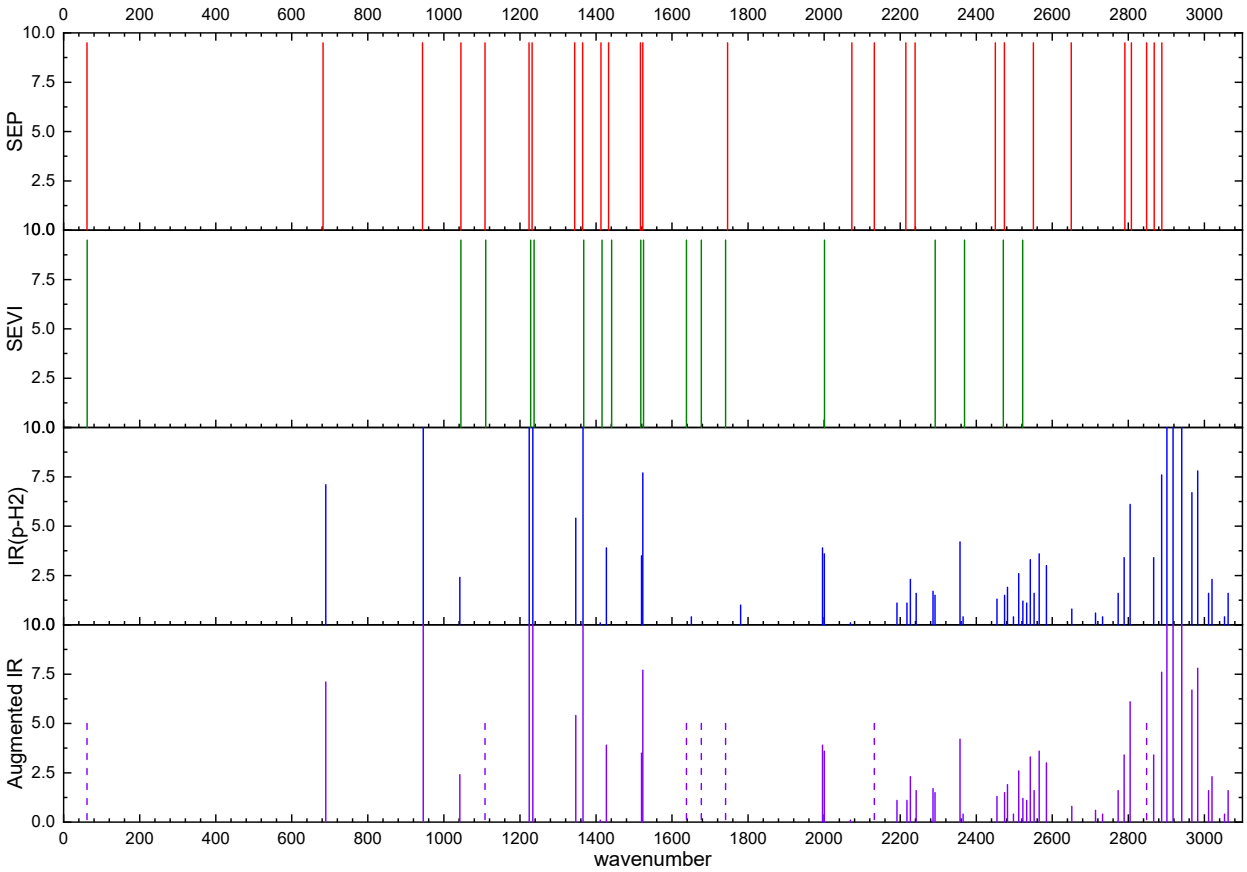

Figure 1: Stick Diagrams Indicating Observed Transitions Frequencies for SEP[22, 23, 25], SEVI[29], Matrix IR[30], and Augmented Matrix IR Spectra in the so Labelled Traces. For the Matrix IR trace the intensities shown are those reported by reference[30]. Values for the off-scale sticks can be found in Table 3. The same is true for the Augmented IR trace, except for those lines not observed in the Matrix IR spectrum. For the small number of the latter transitions (indicated by dashed lines) the intensities are arbitrarily set at half the maximum scale value of 10, as it is impossible to compare intensities among the three experiments.

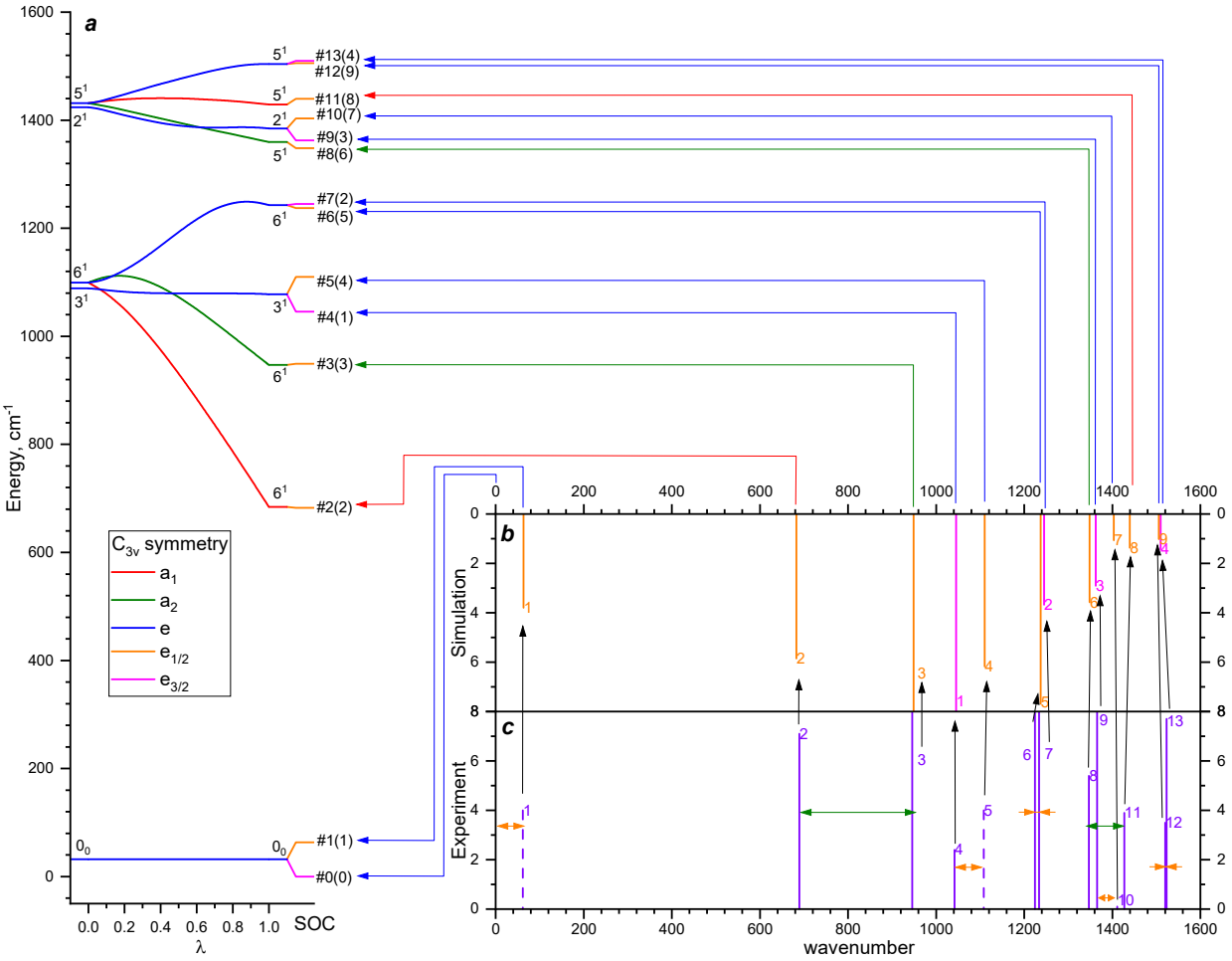

Figure 2: Methoxy energy level diagram (a) and IR absorption spectrum from 0 to 1600 cm^{-1} (b, c). Part (a) panel shows vibronic energy levels depending on the strength of the Jahn-Teller coupling varying via the λ parameter (*See text for details*). At the terminal points, $\lambda = 0$ and $\lambda = 1$, the levels are labeled by the basis functions with the maximum contribution in corresponding eigenvectors. The avoided crossing rule is used to adiabatically track the corresponding vibronic eigenenergies according to which irreducible representation their eigenvectors transform. Extending beyond the $\lambda = 1$ point, the spin-vibronic levels that originate from respective the vibronic levels are shown. Part (b) shows the simulated spin-vibronic transitions associated with the respective energy levels in part (a). The intensities of the transitions are taken from the calculated values given in Table 3. Part (c) shows the experimental spectrum with the assignments to the simulated transitions in part (b) indicated. The simulated transition intensities in part (b) are normalized to line #3 in the experiment [30] (13.0 km·mol^{-1}). The double-headed arrows in part (c) have lengths equal to the simulated energy gaps corresponding to the spin-orbit splitting of e vibronic levels into $e_{3/2}$-$e_{1/2}$ pairs (orange, anchored to the $e_{3/2}$ level) or spin-vibronic energy separation between the $e_{1/2}$-$e_{1/2}$ levels originating from the a_1 and a_2 vibronic levels (green, anchored to the $e_{1/2}(a_1)$ level), respectively.

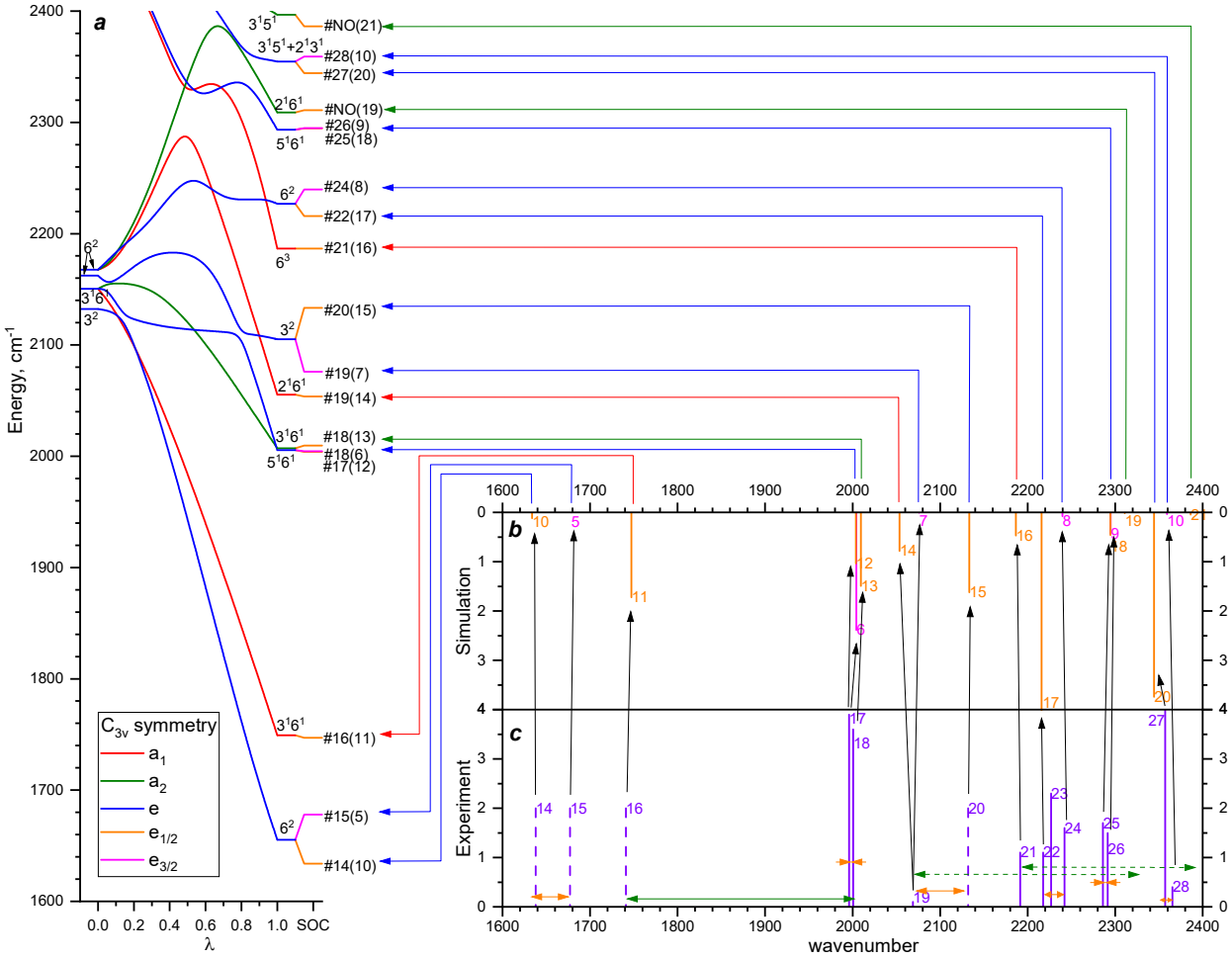

Figure 3: Methoxy energy level diagram (a) and IR absorption spectrum from 1600 to 2400 cm^{-1} (b, c). Additional details are the same as for Fig. 2

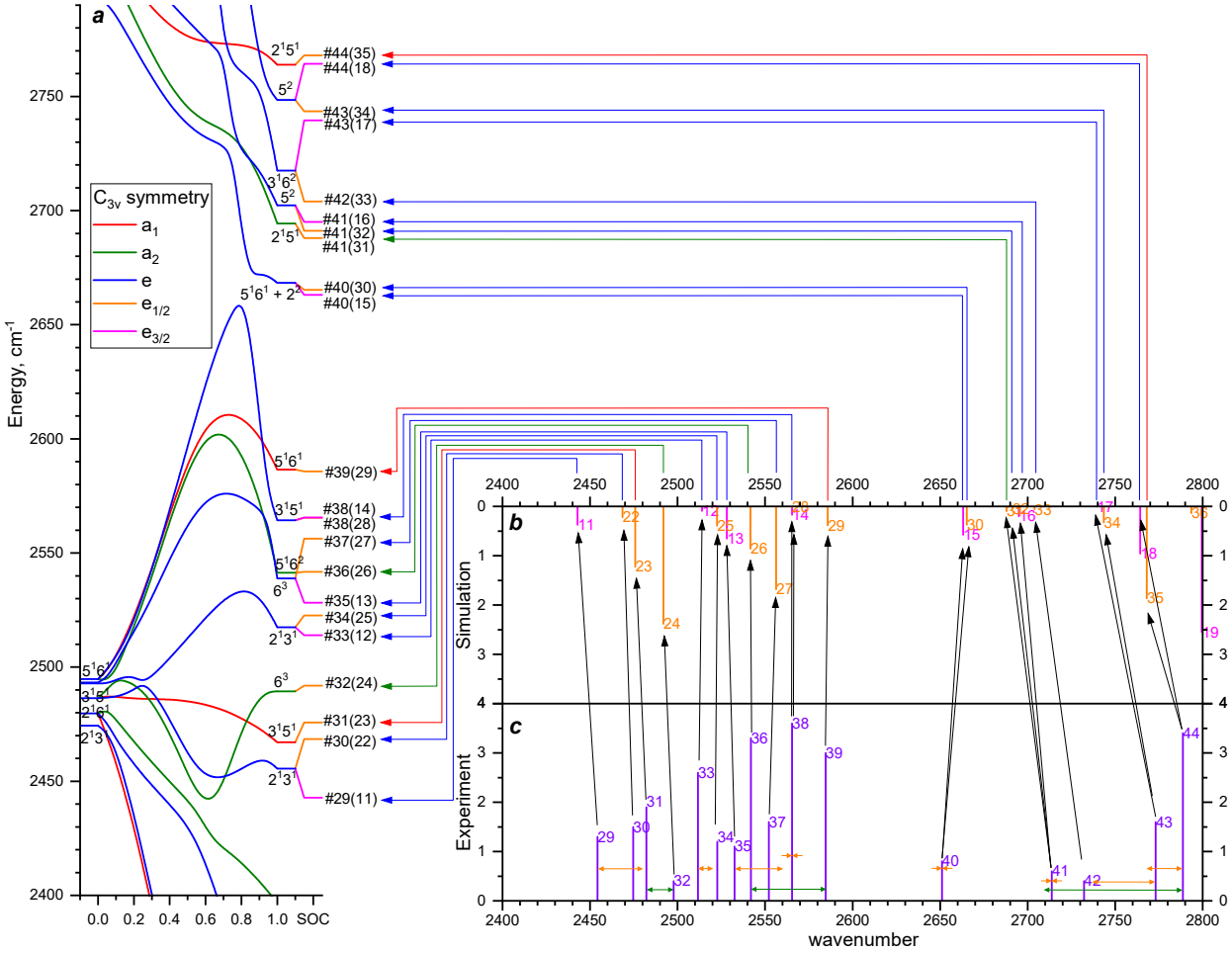

Figure 4: Methoxy energy level diagram (a) and IR absorption spectrum from 2400 to 2800 cm^{-1} (b, c). Additional details are the same as for Fig. 2

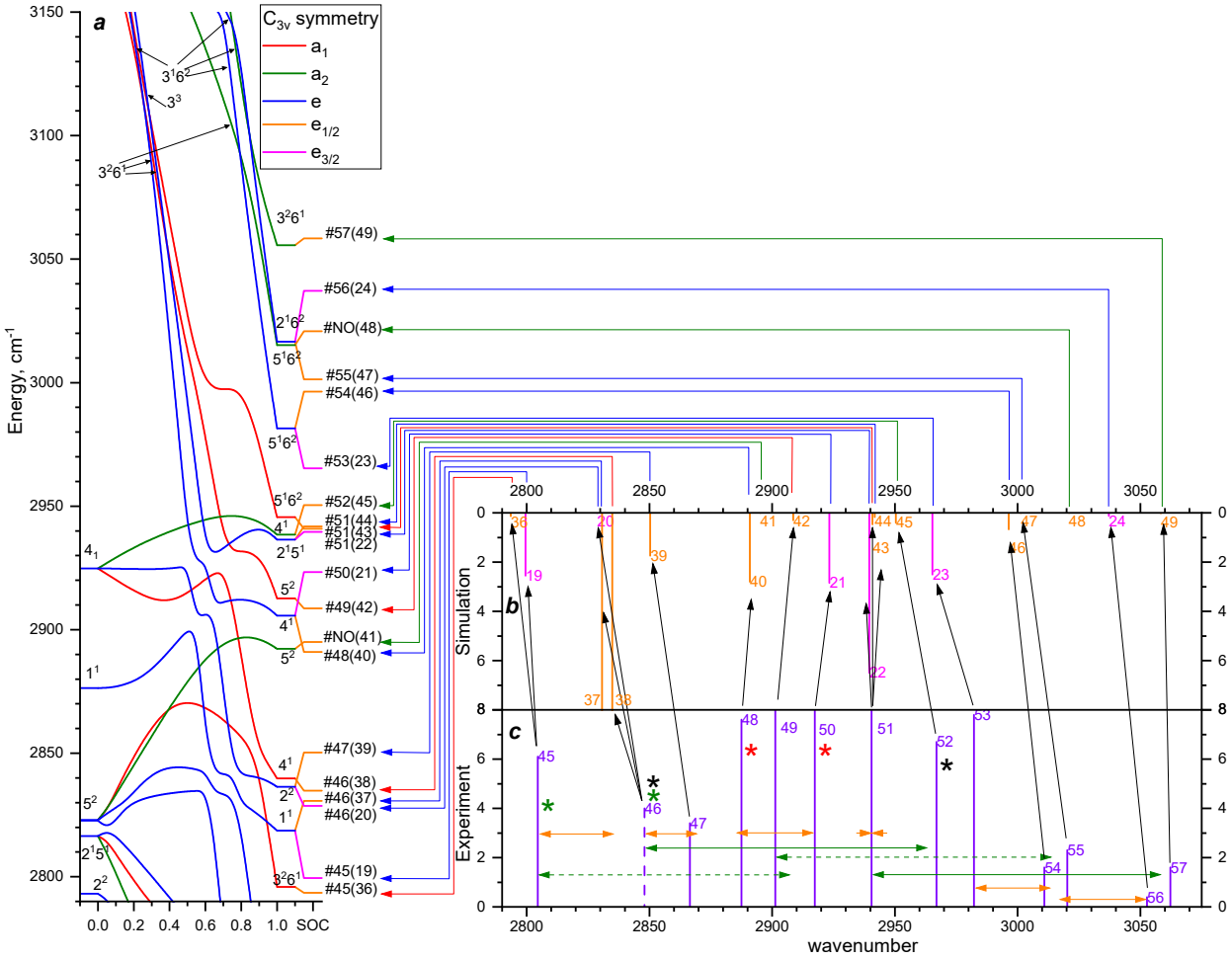

Figure 5: Methoxy energy level diagram (a) and IR absorption spectrum from 2800 to 3075 cm^{-1} (b, c). Additional details are the same as for Fig. 2

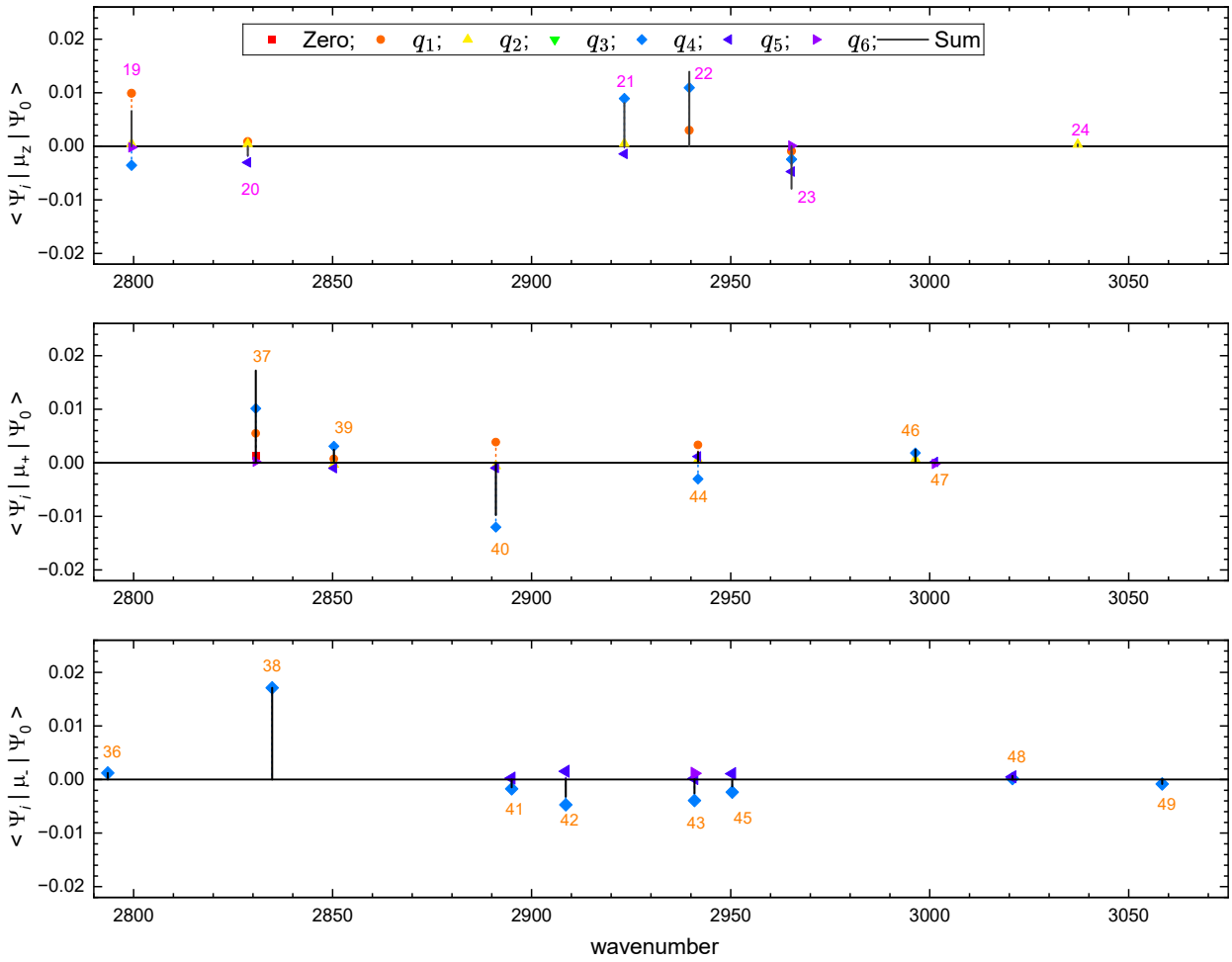

Figure 6: Contributions of the major terms associated with the indicated normal modes to the transition dipole moment matrix elements. A dashed line with a symbol at its termination corresponds to the value of an individual term in Eq. (13) as indicated in the legend: $\sum_{ij} M_{\alpha}^{ij(0)} \langle \tilde{\eta}^i_{n',\Gamma'} | \tilde{\eta}^j_{n'',\Gamma''} \rangle$ for the zeroth order term, $\sum_{ij} M_{\alpha,k}^{ij(1)} \langle \tilde{\eta}^i_{n',\Gamma'} | q_k | \tilde{\eta}^j_{n'',\Gamma''} \rangle$ for a term associated with a mode q_k. The contributions from two components of a doubly degenerate mode are summed, for example, $\sum_{ij} \left(M_{\alpha,4+}^{ij(1)} \langle \tilde{\eta}^i_{n',\Gamma'} | q_{4+} | \tilde{\eta}^j_{n'',\Gamma''} \rangle + M_{\alpha,4-}^{ij(1)} \langle \tilde{\eta}^i_{n',\Gamma'} | q_{-} | \tilde{\eta}^j_{n'',\Gamma''} \rangle \right)$. Solid lines overlaying the dashed lines show the total value of the μ_z, μ_+, or μ_- spin-vibronic transition dipole moment matrix elements. The numbers on the lines correspond to those in the first column of Table 3 that label the simulated energy levels.